JGR Earth Surface

RESEARCH ARTICLE
10.1029/2021JF006141

Glacial Catchment Erosion From Detrital Zircon (U-Th)/He Thermochronology: Patagonian Andes

S. Falkowski[1], T. A. Ehlers[1], A. Madella[1], C. Glotzbach[1], V. Georgieva[2], and M. R. Strecker[3]

[1]Department of Geosciences, University of Tübingen, Tübingen, Germany, [2]Institute for Earth Sciences/Institute of Physics and Mathematics, Universidad Austral de Chile, Valdivia, Chile, [3]Institute of Geosciences, University of Potsdam, Potsdam, Germany

Key Points:

- Integration of bedrock, detrital moraine, and fluvial thermochronometer samples documents spatial variations in catchment erosion
- Approximately 2.5 ka (or earlier) glacial erosion is focused at the Last Glacial Maximum equilibrium line altitude and limited at higher elevations
- A well-constrained bedrock map of cooling ages is essential for quantifying erosion and sediment routing within catchments

Supporting Information:

Supporting Information may be found in the online version of this article.

Correspondence to:

S. Falkowski,
sarah.falkowski@uni-tuebingen.de

Citation:

Falkowski, S., Ehlers, T. A., Madella, A., Glotzbach, C., Georgieva, V., & Strecker, M. R. (2021). Glacial catchment erosion from detrital zircon (U-Th)/He thermochronology: Patagonian Andes. *Journal of Geophysical Research: Earth Surface*, *126*, e2021JF006141. https://doi.org/10.1029/2021JF006141

Received 26 FEB 2021
Accepted 29 SEP 2021

Abstract Alpine glacial erosion exerts a first-order control on mountain topography and sediment production, but its mechanisms are poorly understood. Observational data capable of testing glacial erosion and transport laws in glacial models are mostly lacking. New insights, however, can be gained from detrital tracer thermochronology. Detrital tracer thermochronology works on the premise that thermochronometer bedrock ages vary systematically with elevation, and that detrital downstream samples can be used to infer the source elevation sectors of sediments. We analyze six new detrital samples of different grain sizes (sand and pebbles) from glacial deposits and the modern river channel integrated with data from 18 previously analyzed bedrock samples from an elevation transect in the Leones Valley, Northern Patagonian Icefield, Chile (46.7°S). We present 622 new detrital zircon (U-Th)/He (ZHe) single-grain analyses and 22 new bedrock ZHe analyses for two of the bedrock samples to determine age reproducibility. Results suggest that glacial erosion was focused at and below the Last Glacial Maximum and neoglacial equilibrium line altitudes, supporting previous modeling studies. Furthermore, grain age distributions from different grain sizes (sand, pebbles) might indicate differences in erosion mechanisms, including mass movements at steep glacial valley walls. Finally, our results highlight complications and opportunities in assessing glacigenic environments, such as dynamics of sediment production, transport, transient storage, and final deposition, that arise from settings with large glacio-fluvial catchments.

Plain Language Summary Mountain glaciers flow down valleys and erode the underlying rocks. Furthermore, rivers that are fed by glaciers, rock falls, and hillslope processes contribute to the erosion of glaciated landscapes. Understanding these processes and where erosion occurs in a catchment is important because these factors affect how landscapes evolve over time and under changing climate conditions. It is difficult to directly study processes that occur under glaciers because these regions are inaccessible. As a result, computer models of glacier erosion are often used to predict where and how erosion occurs. One technique to test these models is to trace where sediments, that were deposited in a glacial moraine or that are being transported by a river from a glacier, originated from within the catchment. We applied this technique to moraine and river samples from the Northern Patagonian Icefield, Chile, to determine at what elevation most erosion occurred during neoglacial times, 2.5 thousand years ago, and to better understand the influence of sediment size and sampling location along a river on study results. Our main finding confirms previous computer models and observational studies that erosion during glacial times is focused in a narrow elevation sector, where glacier sliding velocity is highest.

1. Introduction

Alpine glacial erosion exerts a first-order control on mountain topography and sediment production. Glacial erosion has been linked with increased global sedimentation rates since the Pliocene, as well as in the construction, but also destruction, of high mountain relief (e.g., Alley et al., 2019; Champagnac et al., 2014; Egholm et al., 2009; Hallet et al., 1996; Herman & Champagnac, 2016; Leutelt, 1932; Melnick & Echtler, 2006; Sternai et al., 2013; Thomson et al., 2010; Valla et al., 2011). Both observations and numerical models identified different climate, tectonic, and geomorphic conditions, under which glacial and glacio-fluvial processes are most efficient at excavating rocks from landscapes or individual catchments over short (10^1 to

10^2–10^3 years) to long (10^4–10^6 years) timescales (e.g., Bernard et al., 2020; Egholm et al., 2012; Herman et al., 2011, 2015; Koppes et al., 2015; Riihimaki et al., 2005; Yanites & Ehlers, 2012, 2016). Furthermore, numerical models were used to study glacier properties, such as basal sliding velocity or concentration of intra- and subglacial debris, with regard to erosion mechanisms and their rates. Nevertheless, these mechanisms are poorly understood and the uncertain distribution of subglacial erosion and temporal variations in glacial mechanics complicate investigations (e.g., Fernandez et al., 2011; Herman et al., 2011; Humphrey & Raymond, 1994; Ugelvig & Egholm, 2018). Observational data capable of testing model predictions of glacial erosion and sediment production are limited, and so far derive largely from thermochronologic methods (Clinger et al., 2020; Ehlers et al., 2015; Enkelmann & Ehlers, 2015; Stock et al., 2006; Tranel et al., 2011) and Raman spectroscopy of carbonaceous material to track the provenance of eroded material below glaciers (Herman et al., 2015; Jiao et al., 2018).

One technique for observing patterns of catchment erosion is called "tracer thermochronology" (McPhillips & Brandon, 2010). Previous studies documented both the potential and complications associated with using this technique to quantify surface processes and catchment erosion (e.g., Brewer et al., 2003). The underlying concept of tracer thermochronology is based on three parts (cf., Stock et al., 2006). First, a bedrock age-elevation profile is required to document the elevations over which observed ages are sourced from. Second, a detrital sample is collected (e.g., from fluvial, glacial, or hillslope sediments) and the grain-age distribution is measured. Third, the observed detrital grain age distribution is interpreted for the location from which the sediment was sourced based on the observed (or modeled, e.g., Clinger et al., 2020; Whipp & Ehlers, 2019) bedrock ages. Tracer thermochronology has been used as a provenance tool in a variety of studies in present-day fluvial, hillslope, glacial, and deglaciated settings (Clinger et al., 2020; Ehlers et al., 2015; Fox et al., 2015; Glotzbach et al., 2013, 2018; Lang et al., 2018; McPhillips & Brandon, 2010; Reiners et al., 2007; Riebe et al., 2015; Stock et al., 2006; Tranel et al., 2011; Vermeesch, 2007). Different methods have been used to interpolate bedrock age data, or compare predicted and observed age distributions (e.g., Glotzbach et al., 2013; Riebe et al., 2015; Stock et al., 2006; Vermeesch, 2007) and caveats such as heterogeneous mineral fertility or grain size effects on the age distributions have been investigated (Glotzbach et al., 2018; Lukens et al., 2020; Riebe et al., 2015; Tranel et al., 2011).

In the absence of a well-constrained bedrock age-elevation profile (e.g., due to limited field access), other field and modeling studies successfully applied detrital thermochronology to map out potential regional zones of rapid exhumation under glaciers (e.g., Bendick & Ehlers, 2014; Enkelmann et al., 2009, 2015; Falkowski & Enkelmann, 2016; Grabowski et al., 2013). However, without a bedrock age-elevation profile within the catchment, identification of the distribution of erosion is difficult. Despite the advances of previous studies for understanding catchment geomorphic processes, few studies to date have applied tracer thermochronology to glaciated settings (Clinger et al., 2020; Ehlers et al., 2015; Glotzbach et al., 2013; Lang et al., 2018; Stock et al., 2006; Tranel et al., 2011), and our knowledge of where modern or ancient glaciers derived sediment from is incomplete. Tracer thermochronology observations are needed to evaluate glacial erosion and transport laws used in process-based glacial surface process models (e.g., Bernard et al., 2020; Braun et al., 1999; Headley & Ehlers, 2015; Herman & Braun, 2008; Herman et al., 2011; MacGregor et al., 2009; Tomkin & Braun, 2002; Yanites & Ehlers, 2016).

In this study, we contribute with the first application of zircon (U-Th)/He (ZHe) tracer thermochronology data from the heavily glaciated Patagonian Andes. We present six detrital samples from a glaciated catchment in the Northern Patagonian Icefield, Chile (46.7°S; Figure 1). In contrast to previous applications of detrital apatite (U-Th)/He (AHe) thermochronometry, we apply detrital ZHe thermochronometry due to better bedrock ZHe age reproducibility and larger age range in the age-elevation relationship. This facilitates a more robust interpretation of results. Furthermore, due to the resistance of zircons they are more abundant in metasediments and less prone to abrasion during transport than apatites.

More specifically, we apply tracer thermochronology to test three hypotheses: (1) if erosion is most efficient around the glacial equilibrium line altitude (ELA, i.e., average elevation over one-year time, where ablation equals accumulation) due to high ice sliding velocities, then the observed distribution of detrital ages should reflect ELA elevations. To test this, we determine the elevation distribution of erosion reflected by the distribution of cooling ages from a moraine sample; (2) if surface and/or tectonic processes vary along the length of a valley, then these variations should be reflected in changes in the downstream detrital age

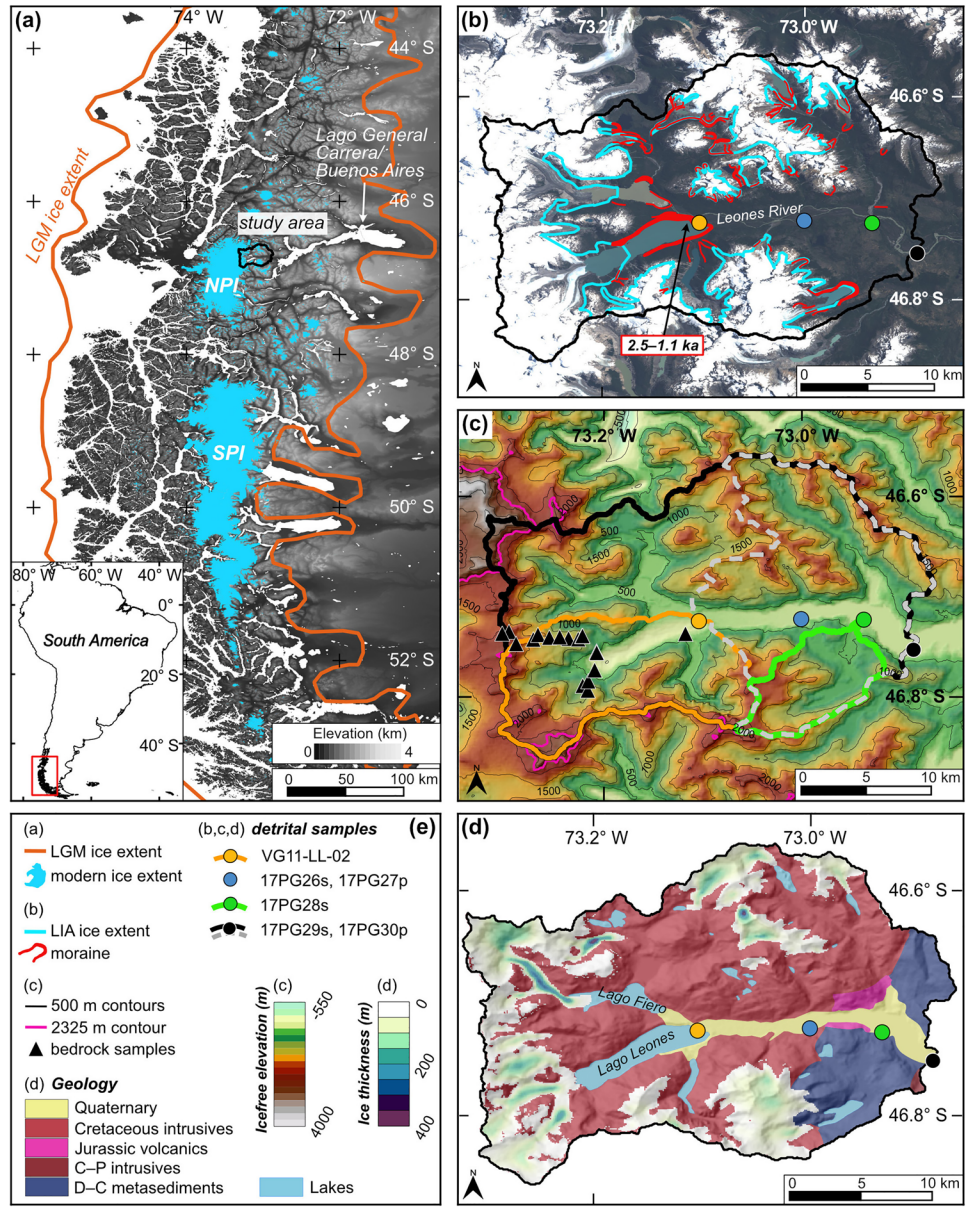

Figure 1. Topographic and geological overview of the study area in Southern Patagonia. (a) Topographic map based on the SRTM 90 m DEM (Shuttle Radar Topography Mission digital elevation model; NASA); map extent indicated by red box in inset. White is water. Last Glacial Maximum (LGM) ice extent after Caldenius (1932) and Clapperton (1993), modern ice extent from GLIMS glacier database (GLIMS Consortium, 2005; Raup et al., 2007). NPI, SPI: Northern and Southern Patagonian Icefield, respectively. (b) Landsat8 satellite image of the northeastern NPI including the study area. Little Ice Age (LIA, ~1870 CE) ice extent from GLIMS glacier database (Davies & Glasser, 2012); location of moraines from Harrison et al. (2008) and Glasser et al. (2012). Age of the Lago Leones terminal moraine (in box) from Harrison et al. (2008). (c) Ice-free DEM of the study area (ice was subtracted based on ice thickness data from Carrivick et al., 2016). Water and moraine ridges from Lago Leones were also subtracted based on bathymetry data from Haresign and Warren (2005). The 2,325 m contour line represents the highest sample elevation of bedrock samples (Georgieva et al., 2016, 2019). Detrital sample locations are shown with catchment outlines (entire catchment in black and catchment without area behind Leones and Fiero lakes in dashed gray for 17PG29s/-30p; catchment outline for trunk stream samples 17PG26s/-27p left out for clarity of presentation). (d) Geological map of the study area (SERNAGEOMIN, 2003), overlaid by modern ice thickness (Carrivick et al., 2016) and hillshade. (e) Legends for a–d.

distribution. We test this hypothesis by comparing grain age distributions from samples collected along ~11 km of the modern fluvial channel, downstream of the moraine sample; and, finally, (3) if glacial and periglacial bedrock erosion mechanisms such as abrasion, quarrying/plucking, or rockfall onto the glacier have different spatial distributions and produce sediments of different grain sizes, then differences in the pattern of erosion should be detectable by analyzing different grain sizes.

Considering hypothesis (3), for example, coarse sediments (pebbles and coarser) could originate from plucked bedrock from the base of a glacier, or from mass movements such as rockfalls or landslides onto a glacier. Finer sediments (sand and finer) are expected to originate preferentially from the base of a glacier due to abrasion, which is proportional to ice sliding velocity. Comminution of coarse sediments during transport complicates a potential signal, but the presence or absence of differences between age distributions in different grain sizes from sample locations at different transport length can test this hypothesis. To do this, we compare age distributions from sand- (63–250 μm) and pebble-sized (~2–4 cm) sample pairs from two locations in the fluvial channel.

2. Study Area

2.1. Glacial History

The study area is located at the northeastern flank of the Northern Patagonian Icefield and comprises the Leones and Fiero outlet glaciers that both terminate in proglacial lakes (Figure 1). Glaciation in Patagonia began at least at 7 Ma and several ice advances have been identified and dated with the most extensive one probably being the 1 Ma Great Patagonian Glaciation (e.g., Caldenius, 1932; Davies & Glasser, 2012; Davies et al., 2020, and references therein; Hein et al., 2011; Mercer, 1976; Singer et al., 2004). The Last Glacial Maximum (LGM, ~18 ka), Little Ice Age (LIA, ~1870 CE), and modern ice extents are shown in Figure 1. After the Antarctic Cold Reversal (~13 ka), glaciers retreated rapidly to their present limits until the onset of neoglacial readvances at ~5 ka (Clapperton, 1983; Davies et al., 2020, and references therein; Mercer, 1976). Near the eastern end of the Leones Valley, a moraine was dated at ~11.5 ka indicating the study area was still fully glaciated by this time (Glasser et al., 2012). The ~135-m-high terminal moraine that dams Lago Leones was dated by cosmogenic nuclide and optically stimulated luminescence methods at ~2.5–1.1 ka (Harrison et al., 2008). Three submerged moraine ridges within the 10-km-long and 2.5-km-wide Lago Leones represent further glacier recessions (Haresign & Warren, 2005; Harrison et al., 2008). The terminal moraine damming Lago Fiero has not been dated but is older than the LIA and possibly younger than or of the same age as the Lago Leones moraine (Figure 1b). Most other preserved moraines coincide with the LIA ice extent and in many cases dam lakes at >500 m elevation (Figure 1b). The present-day ELA is at ~1,350 m (Rivera et al., 2007); it was thus lowered by 750–950 m during the LGM (LGM ELA at 400–600 m; Hubbard et al., 2005).

The Lago Leones terminal moraine sampled for this study constitutes material eroded and transported by the Leones Glacier (Figures 1b–1d). The moraine is mainly composed of sandy boulder gravel and sandy gravel (Harrison et al., 2008). The ELA during the time of deposition of the moraine was presumably between the modern and LGM ELA. The Leones Glacier today constitutes three, mostly debris-free tributaries that join below a 1.5-km-wide ice cliff at ~750 m elevation; the glacier terminates at Lago Leones at 315 m elevation. Lago Leones is up to 350 m deep and occupies an overdeepened part of the Leones Valley (Haresign & Warren, 2005; Harrison et al., 2008). The thickness of sediments filling the Leones Valley, which is occupied by the Leones River, is unknown.

2.2. Geology

The majority (~80%) of the study area (western part) exposes granitoids of the Cretaceous Patagonian Batholith (SERNAGEOMIN, 2003). The remaining 20% of the Leones Valley is predominantly covered by Devonian–Carboniferous metasediments with intrusions of Cretaceous igneous rocks, some Jurassic volcanics, and a minor occurrence of Carboniferous–Permian intrusives (Figure 1d). The ice cover hinders detailed geologic mapping of the western part of the catchment and it cannot be ruled out that some metasediments are also exposed underneath the ice. More specifically, we determined at sampling location 17PG26s/-27p (Figure 1d) that at least 21% of the pebbles present were from metamorphic lithologies (Figure 2a). The site

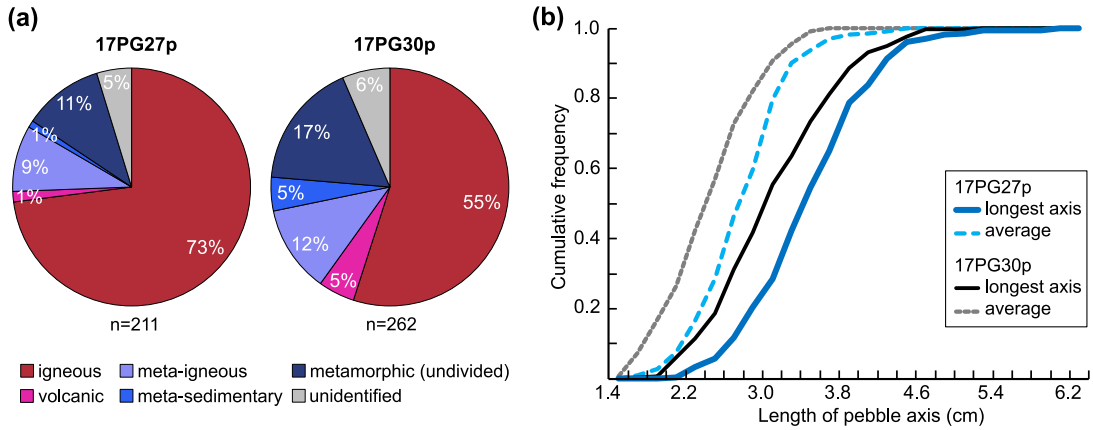

Figure 2. Lithology and grain size of pebble samples 17PG27p and 17PG30p. Thermochronometric analyses were conducted on the crushed and sieved size fraction of 63–250 μm. (a) Pie charts of pebble lithologies. *n*: number of pebbles. (b) Cumulative frequency of average (three measurements per pebble) and longest axes of pebbles. Grain size distribution reflects the ~2–4 cm size range sampled, rather than the full distribution of clast sizes present at the sampling location (see Section 3.1 for details). For data see Table S1 in Falkowski et al. (2021).

is close to the southwest-northeast trending contact between granitoids and metasediments. Either those 21% of metamorphic pebbles were derived locally, or there are unmapped exposures of metamorphic rocks east of the mentioned contact.

All available bedrock samples are from granitoids from the Leones Glacier catchment, the westernmost part of the Leones Valley with the highest topography (cf., yellow outline in Figures 1c and 1d; Georgieva et al., 2016, 2019). This means that we do not have direct observations from bedrock of the other lithologies with regard to zircon fertility. Zircon fertility describes the propensity of source rocks to contribute detrital zircons when eroded. This can be variable within and between lithologies and can have an important impact on the interpretation of age distributions in any provenance study (e.g., Chew et al., 2020; Malusà et al., 2016). All granitoid bedrock samples yielded abundant zircons, and one of our detrital fluvial samples from a tributary underlain by metasediments yielded abundant zircons as well (green outline in Figure 1c, 17PG28s). Given this, we conclude zircon fertility is likely not a source of bias in this study.

Lastly, no faults have been mapped within the study area or are visible in satellite images, but dense vegetation in the region hampers a rigorous evaluation of neotectonic features. The presence of faults, if not accounted for, could offset age-elevation relationships of bedrock thermochronometric ages and result in errors in the interpolation of bedrock ages over the catchment. However, as will be explained below in Section 5.1, we use an interpolation of bedrock ages only for the Leones Glacier catchment, where the age-elevation relationship is well constrained from available bedrock samples. Thus, there is no bias from the potential presence of unmapped faults.

3. Samples and Methods

3.1. Detrital and Bedrock Samples

We collected six detrital samples along ~19 km of the Leones Valley. These samples include one sample from the ~2.5 to 1.1-kyr-old terminal moraine damming Lago Leones (VG11-LL-02; cf., Section 2.1) and five fluvial sediment samples from three locations in the modern river channel (Figures 1b–1d, Table 1). Representative photographs of the sample locations are shown in Figure S1 in Supporting Information S1.

The ~16 kg moraine sample is a mixture of material from the interior of the moraine and was collected at four different locations. Those four locations were equally distributed along the lakeward flank of the moraine, a sampling strategy that was also recently suggested based on data of modeled transport paths of detritus within a glacier (Bernard et al., 2020). We therefore assume that the sample is representative for the entire catchment. The grain sizes of the sample material were mainly very fine to coarse sand and granules,

Table 1
Sample Locations and Catchment Characteristics

Sample id	Sample type, grain size	Longitude (dd)[c]	Latitude (dd)[c]	Elevation (m)	Catchment elevation range (m)[d,e]	Catchment area (km²)[e]
VG11-LL-02	Terminal moraine, mainly sand[a]	−46.7251	−73.1031	428	−1–2,908	208
17PG26s	Modern trunk river, sand[a]	−46.7223	−73.0007	238	−1–3,630	530
					235–2,047	94
17PG27p	Modern trunk river, pebbles[b]	−46.7223	−73.0007	238	−1–3,630	530
					235–2,047	94
17PG28s	Modern tributary river, sand[a]	−46.7242	−72.9328	235	235–2,245	79
17PG29s	Modern trunk river, sand[a]	−46.7554	−72.8831	235	−1–3,630	786
					235–2,245	350
17PG30p	Modern trunk river, pebbles[b]	−46.7554	−72.8831	235	−1–3,630	786
					235–2,245	350

[a]Sand samples were sieved to 63–250 μm in the laboratory. See Section 3.1 for details on the moraine sample. [b]For individual pebble sizes see Table S1 in Falkowski et al. (2021). Pebbles were crushed per sample and sieved to 63–250 μm. [c]WGS-84. [d]Based on an SRTM 90 m digital elevation model downsampled to 500 m horizontal resolution, as used in our analyses. [e]For the modern river samples, elevation range and catchment area are given for the entire upstream catchment (upper row per sample) and the upstream catchment excluding the area upstream of Leones and Fiero lakes (lower row per sample).

with some fine to coarse pebbles (grain size after Wentworth, 1922). The bulk sample was processed for mineral separation.

Two additional samples were collected at ~7.5 km and ~19 km downstream of the sampled moraine in the main (trunk) river. The Leones River is a braided stream occupying the 1–2-km-wide valley and terminates with an almost 5-km-wide delta at Lago General Carrera/Buenos Aires (~28 km downstream of the sampled moraine, Figure 1a). At each sample location, both a sand and a pebble sample were collected (17PG26s and 17PG27p, and 17PG29s and 17PG30p, where "s" stands for sand and "p" for pebbles). One additional sand sample was collected from a tributary in the southeastern part of the catchment, ~13.5 km downstream of the sampled moraine (17PG28s; Figure 1c). Due to limited field access, it was impossible to sample elevations above the trunk valley floor; therefore, tributary sample 17PG28s was collected at the same elevation as the modern trunk samples (Table 1, Figure 1). Consequently, we cannot entirely rule out sediment input from the main valley (from the infill or modern trunk stream). However, the criteria for the sampling location (a sand/pebble bank within the tributary stream, which was ~25 m wide and had a relatively strong current at that location) were adapted to minimize this possibility. Accordingly, we assume that the sample was sourced from the tributary catchment as outlined in Figure 1c (green line).

Sand and pebble samples were collected as mixtures from several locations along tens of meters within the modern river on point bars or sand/pebble bars. About 8 kg of sand was collected at each location. Coarse to very coarse pebbles (after Wentworth, 1922) were collected at each location considering the fraction of pebble lithologies at each site (Figure 2a). To do this, we estimated the percentage of pebble lithologies present and collected pebbles accordingly. We did not conduct point counting. The goal was to collect >200 pebbles of the same size at both sample locations, which resulted in a ~2–4 cm size range (Figure 2, Table S1 in Falkowski et al. [2021]). Due to the time-intensive nature of our conventional whole-grain ZHe analysis (Section 3.2.1), we chose to capture differences between two grain size fractions (sand and pebbles).

Bedrock samples from an elevation transect in the Leones Glacier catchment are available from previous studies with apatite (U-Th)/He and fission track data (Georgieva et al., 2016, 2019), and ZHe and zircon fission track data (Figure 3a; Andrić-Tomašević et al., 2021). The 18 granitoid bedrock samples analyzed for ZHe originated from elevations between 326 and 2,325 m. Three to four ZHe single-grain ages were analyzed from each sample. Because bedrock thermochronometric age uncertainty is determined in terms of single-grain age reproducibility, which is not possible to conduct on detrital single-grain ages, we selected two bedrock samples to evaluate single-grain age reproducibility to later apply to detrital grain-age uncertainties. For this, we chose samples from a high (2,080 m) and low (326 m) elevation to measure an additional

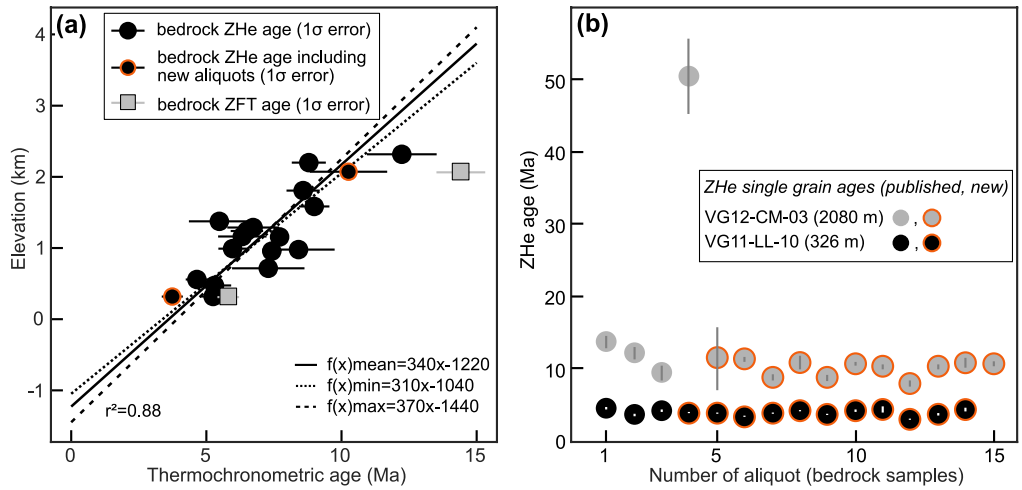

Figure 3. Available bedrock zircon (U-Th)/He (ZHe) and zircon fission track (ZFT) thermochronometric ages (Andrić-Tomašević et al., 2021; sample locations in Figure 1c) and new bedrock ZHe single-grain ages. (a) ZHe age-elevation relationship of the vertical sample profile and ZFT ages. (b) Published and new ZHe single-grain ages (with 1σ analytical uncertainties) of two samples that we used to evaluate single-grain age reproducibility. Data are shown in Tables S2 and S3 in Falkowski et al. (2021).

11 aliquots for each (Figure 3b). Those new thermochronometric ages are included in the bedrock mean age calculations and determination of the age-elevation relationship (Figure 3a).

3.2. Zircon (U-Th)/He Tracer Thermochronology

3.2.1. Zircon (U-Th)/He Analyses

The moraine sample was crushed, milled and sieved to 63–250 μm before density and magnetic separations of minerals at the University of Potsdam, Germany. The modern river sand samples were sieved to 63–250 μm grain size before density and magnetic separations at the University of Tübingen, Germany. This size fraction of sand generally contains most zircons, the zircons are of sufficient size for the necessary alpha-ejection correction (Farley et al., 1996), and aeolian input, if present, is minimized. The lithology of individual pebbles was determined and their axes were measured three times per pebble with a caliper (short, intermediate, and long axis; Figure 2, Table S1 in Falkowski et al. [2021]). All pebbles from a sample were crushed together, then sieved to 63–250 μm and further separated by density and magnetic techniques in Tübingen.

Mineral separates of new detrital samples and previous bedrock samples were then picked for suitable zircons at 256X magnification under reflected and transmitted light. Criteria for picking bedrock zircons include transparency, no or only a few small inclusions, no fractures or broken parts, idiomorphic crystal habit, grain diameter of >80 μm, and similar size of crystals for each sample (e.g., Reiners, 2005). Zircon quality and abundance was high in bedrock samples such that we could pick ideal crystals. Grain selection in detrital samples must be carefully considered to not bias results by only selecting one zircon population for measurements. We did not encounter zircon morphologies or colors that we did not see in bedrock samples. We aimed at picking ~100 zircons of sizes, crystal habits, and colors (clear to reddish) present in each sample. The quality and abundance of zircon grains was overall high, such that we could pick grains that fulfilled most of the criteria used in the bedrock zircon picking. This is particularly important because we applied the conventional ZHe analytical method that involves the dissolution of whole grains in acids. If, for example, grain fragments and rounded grains needed to be measured, laser ablation-based methods (*in-situ* measurements) could be more suitable (Tripathy-Lang et al., 2013).

Selected zircons were photographed four times, parallel and perpendicular to the crystallographic c-axis, then packed in niobium tubes for measurement in a Patterson helium-line. Subsequently, packed grains were spiked with ^{233}U and ^{230}Th solutions and we employed a two-step HF + HNO_3 and HCl high-pressure

digestion procedure. The final solutions of 5% HNO_3+0.5% HF were measured with a Thermo Fisher Scientific iCAP Qc inductively coupled plasma quadrupole mass spectrometer at the University of Tübingen. Details can be found in the Supporting Information of Stübner et al. (2016). A difference to the methods described there, is that we calculated grain masses from numerically determined grain volumes and an assumed zircon density of 4.65 g/cm^3 (2% error) after Glotzbach et al. (2019). The numerical determination of three-dimensional grain geometries and alpha-ejection correction factors (F_T factors) to account for non-diffusional helium loss was based on the photographs taken and using the approach of Glotzbach et al. (2019).

3.2.2. Determination of Source Area Elevation and Comparisons Between Detrital Age Distributions

Here we summarize the steps used to infer patterns of upstream catchment erosion from detrital grain-age distributions and the steps for comparison of observed detrital grain-age distributions to each other. We used the *ESD_thermotrace* software (Madella et al., 2021) to (a) predict detrital grain age distributions depending on the bedrock age of the catchment and changes in the pattern of erosion, (b) evaluate the likelihood of drawing the observed detrital samples from these predictions, and (c) quantify the confidence level permitted by the size of our samples. The program was modified to include the display of the erosional distribution/function with elevation, and to allow statistical comparison between two observed cumulative age distributions (CADs). Details are described below.

3.2.2.1. Bedrock Age Map

The 18 bedrock samples described in Section 3.1 exhibit a positive correlation between ZHe age and elevation. The age-elevation relationship (with 95% confidence interval) was constructed by least-square fitting of a straight line and testing for the possibility that the age-elevation relationship is better fitted with more than one slope (after Glotzbach et al., 2011). The age-elevation relationship was employed to map surface bedrock age and related uncertainty to a digital elevation model (DEM, downsampled to 500 m horizontal resolution). The total age uncertainty is based on the single-grain age reproducibility of the bedrock samples and the uncertainty of the linear regression. To obtain an ice-free DEM, we used an SRTM 90 m DEM and subtracted ice thickness data from Carrivick et al. (2016), who derived interpolated first-order estimates of ice thickness by applying a perfect-plasticity model along the glacier center-lines. The uncertainty in the ice thickness, and hence the resulting ice-free DEM, was estimated at 11% (<42 m) (Carrivick et al., 2016). Note that the vertical resolution of the SRTM 90 m DEM is reported to be <16 m absolute (NASA). We also used bathymetry information from Lago Leones (Haresign & Warren, 2005) to subtract elevation values for water and moraine ridges from the DEM. We estimate the uncertainty to be <15%. The bathymetry of Lago Fiero and thickness of sediment infill of the Leones Valley are unknown and not subtracted from the DEM. The difference in original and modified DEMs is illustrated in Figure S2 in Supporting Information S1, where six elevation plots are shown along tributaries in the upstream catchment of the moraine sample. Ice thickness in that part of the Leones Valley is relatively thin (<175 m), whereas removing the water surface of Lago Leones adds the ~0–300 m elevation sector to the DEM and thereby to the bedrock age map. Our analysis shows the importance of the latter (Section 5.2).

3.2.2.2. Predicted Cumulative Age Distributions (CAD) and Best-Fit Elevation Distribution of Erosion

We use the terms "observed" and "predicted" CADs (sorted mean ZHe ages) to refer to the CAD of measured ZHe ages from our detrital sample and to the CAD that is constructed from a sample drawn from the bedrock age map, respectively. To construct predicted CADs, the *ESD_thermotrace* software samples each cell of the bedrock age map, taking a number of ages from a normal distribution centered at the local mean age and scaled according to the interpolation uncertainty. The number of ages drawn for each cell is proportional to the erosional weight that is defined by an erosional function of, for example, elevation (i.e., erosion scenario). A best-fit erosion scenario is determined through minimization of the dissimilarity (i.e., K-S statistic, see below) between predicted and observed CADs by iteratively varying the elevation distribution of erosional weights. For this process, we first clipped the observed detrital age range to exclude ages that do not fall within the range of possible ages based on the bedrock age map, which was clipped to the upstream catchment area of a detrital sample. This step assumes that the bedrock age-elevation profile is

representative of the entire catchment—an assumption we revisit later (Section 5.1). The vertical resolution of the erosional distribution function with elevation is 250 m (based on the slope of the bedrock age-elevation relationship and age uncertainty). When presentation clarity allows, we show CADs with the 95% confidence envelope determined by the sample size. The confidence envelope represents the Dvoretzky-Kiefer-Wolfowitz (DKW) inequality bounds (Massart, 1990). This analytical solution is used in all instances, where a 95% confidence interval is calculated (see below).

3.2.2.3. Dissimilarities Among Age Distributions

All dissimilarities among distributions (either predicted or observed) are calculated using the Kolmogorov-Smirnov (K-S) statistic, which is the maximum absolute vertical distance between two CADs in the observation-cumulative frequency space. For visualization purposes, we additionally show distributions in the form of kernel density estimations (KDEs). The K-S statistic is also used as a metric for dissimilarity in a multidimensional scaling analysis (MDS), where a two-dimensional coordinate system is fit to the matrix of dissimilarity among all observed distributions, such that distances in an MDS plot are a good approximation of the actual difference among distributions (for details see Vermeesch, 2013).

3.2.2.4. Visualization of Comparisons Between Cumulative Age Distributions

We present comparisons between age distributions in several ways. One is the MDS plot described above. Then, we show CADs with the 95% confidence band. If one CAD lies completely within the confidence band of the other, they are indistinguishable at the 95% confidence level. Furthermore, because CADs are constructed by sorting mean ages and ignoring uncertainties, to fully account for analytical uncertainties and sample size, we conduct two-sample tests to determine the likelihood that two observed distributions are drawn from the same underlying population, as follows: given two samples A and B, having sample sizes k_A and k_B and known analytical uncertainties, we first calculate the least significant dissimilarity to A for $n = k_A$ at the 95% confidence level through bootstrapping. Then, we iteratively calculate the likelihood that a random $n = k_B$ subsample of B is as, or less, dissimilar to sample A than the 95% confidence interval of A. Although we do this for measured age distributions that have a known sample size, we show the curves to show whether two samples could be discerned from one another with a high likelihood with even fewer grains than measured (figures presented in Section 5.3).

4. Results

4.1. Bedrock Zircon (U-Th)/He Ages and Reproducibility

A total of 22 new ZHe single-grain data from two of the available bedrock samples (cf., Section 3.1) are presented in Table S2 in Falkowski et al. (2021) and Figure 3b. The new bedrock ZHe mean ages are then 3.7 ± 0.4 Ma and 10.3 ± 1.4 Ma (Figure 3b, Table S3 in Falkowski et al. [2021]). The 1σ age uncertainties are 10.5% and 13.9%, respectively, with 14 single-grain ages in each sample (one single-grain age of ∼50 Ma was excluded as an outlier). The observed bedrock ages range between 3.7 ± 0.4 Ma and 12.2 ± 1.3 Ma between elevations of 326 and 2,325 m (Figure 3a). The weighted average age uncertainty of all bedrock samples is 12.8%. Calculations exclude only the ∼50 Ma grain age of sample VG12-CM-03 (Table S3 in Falkowski et al. [2021], Figure 3b), but include two single-grain ages that were excluded in mean age calculations (6.1 Ma and 16.8 Ma; Table S3 in Falkowski et al. [2021]). In total, 92 single-grain ages are now available from 18 bedrock samples, with only three grains excluded from the bedrock mean age calculation (Table S3 in Falkowski et al. [2021]).

Based on the larger uncertainty of 13.9% of the two samples tested for reproducibility and the weighted average age uncertainty of 12.8%, we conservatively assign a 14% uncertainty to our ZHe ages. The total ZHe age uncertainty to be mapped to the DEM (cf., Section 3.2.2) includes the uncertainty of the age-elevation relationship and varies slightly with elevation between ∼14.5% and ∼16% (total age uncertainty).

4.2. Observed Detrital Zircon (U-Th)/He Age Distributions

A total of 622 detrital ZHe analyses are presented in Table S4 in Falkowski et al. (2021) and Figure 4. Selected grain data such as the ZHe age, analytical and 14% uncertainty (cf., Section 4.1), effective uranium, and

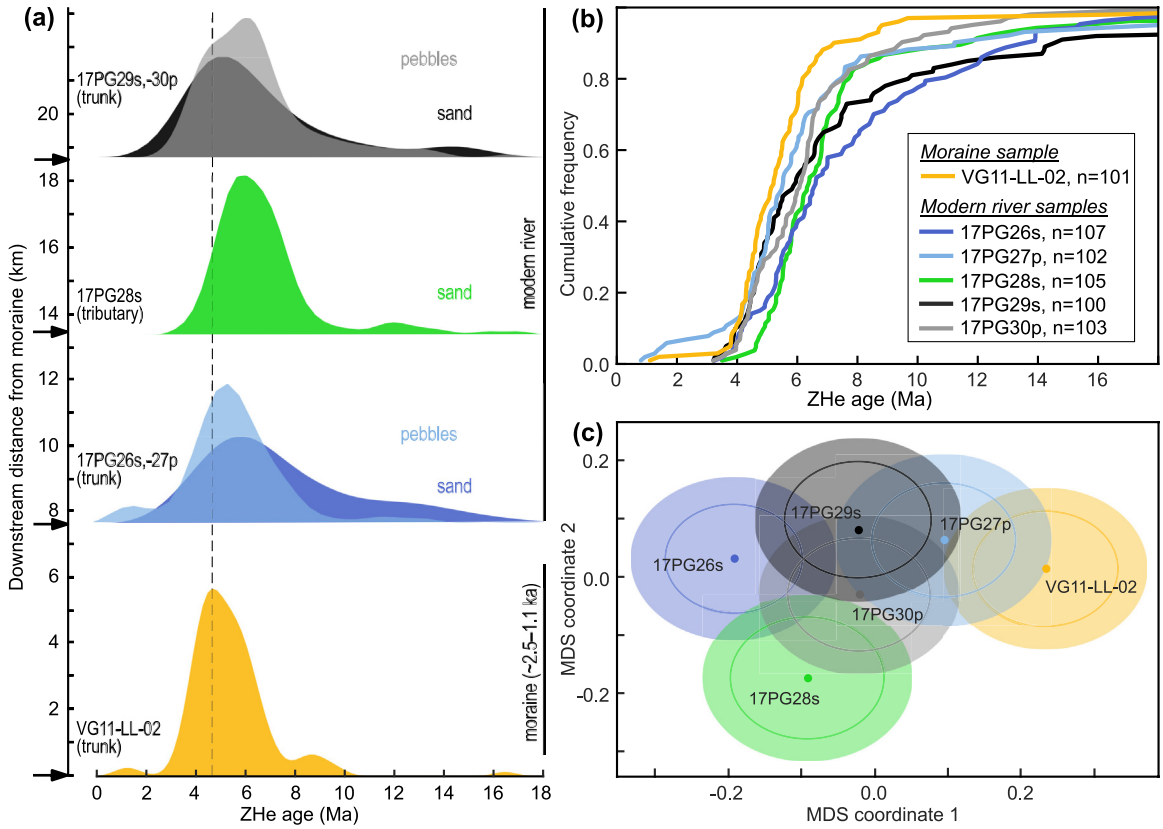

Figure 4. Summary of measured zircon (U-Th)/He (ZHe) detrital ages and their comparison (age axes are clipped at 18 Ma; see Table S4 or Tables S5–S10 in Falkowski et al. [2021] for full age ranges). (a) Kernel density estimations (KDEs) for detrital age distributions shown by downstream sampling distance from the Lago Leones moraine. The dashed line is to guide a comparison between samples. (b) Cumulative age distributions (CADs) of detrital samples. *n*: number of ages. (c) Multidimensional scaling (MDS) plot with 68% (hollow) and 95% (filled) confidence ellipses (see Section 3.2.2 for details on plots).

sphere-equivalent radius for each sample are summarized in Tables S5–S10 in Falkowski et al. (2021). The calculated age distributions are shown in Figure 4 in the form of KDEs (Figure 4a), CADs (Figure 4b), and an MDS plot (Figure 4c). In the following, we describe the observed ages for each sample starting with the moraine and moving downstream.

Detrital ZHe ages for the moraine sample (VG11-LL-02) range from 1.1 ± 0.2 Ma to 22.9 ± 3.2 Ma (14% age error, number of grains $n = 101$, one excluded grain see Table S5 in Falkowski et al. [2021]). No analyses on different grain sizes of this sample are available. The upstream-most fluvial sample location has sand and pebble grain age ranges of 3.2 ± 0.5 Ma to 25.2 ± 3.5 Ma ($n = 107$; 17PG26s) and 0.8 ± 0.1 Ma to 56.4 ± 7.9 Ma ($n = 102$, 17PG27p, one excluded grain see Table S7 in Falkowski et al. [2021]), respectively. The next sand sample downstream is from a tributary stream and has an age range of 3.5 ± 0.5 Ma to 44.8 ± 6.3 Ma ($n = 105$; 17PG28s). The sample location farthest downstream has sand and pebble age ranges of 3.2 ± 0.4 Ma to 47.3 ± 6.6 Ma ($n = 100$; 17PG29s, two excluded grains see Table S9 in Falkowski et al. [2021]) and 3.2 ± 0.4 Ma to 22.9 ± 3.2 Ma ($n = 103$; 17PG30p), respectively.

The exclusion of one zircon grain in sample VG11-LL-02 is based on its low effective uranium content (eU = 9 ppm) and the exclusion of a total of three zircons in samples 17PG27s and 17PG29s is due to their unexpectedly old ages (Tables S7 and S9 in Falkowski et al. [2021]). Here we exclude ages that are older than 60 Ma ($n = 3$; also see Section 5.1) as those are the oldest bedrock ZHe ages observed farther north at approximately the same longitude (Andrić-Tomašević et al., 2021). We do not exclude very young detrital ZHe ages (<2 Ma; $n = 8$; Tables S5 and S7 in Falkowski et al. [2021]) as we do not know how thick the sedimentary infill of the Leones Valley is and some detrital zircons could have been eroded from bedrock elevations currently covered by sediments.

The KDEs of the detrital samples show peaks between ~4.8 Ma (VG11-LL-02) and 6 Ma (17PG30p; Figure 4a), where the moraine sample VG11-LL-02 yielded the overall youngest and 17PG26s the overall oldest age distribution (Figure 4b). The age distributions of the moraine sample, modern river pebble sample 17PG27p and modern river sand sample 17PG28s are relatively narrow, while the others are wider with longer (old age) tails (Figure 4a). The MDS plot illustrates the dissimilarity between the age distributions (cf., Section 3.2.2). For example, the age distribution of VG11-LL-02 is most dissimilar to the age distributions of 17PG26s and 17PG28s and least dissimilar to the age distribution of 17PG27p (Figure 4c).

5. Interpretation

5.1. Evaluation of the Bedrock Age-Elevation Relationship

The analysis of erosion patterns depends on the validity of the bedrock age-elevation relationship and assumed uncertainties in the detrital ages. Here, we evaluate in detail the interpolated bedrock age map before presenting further analyses of the detrital age distributions.

Observed detrital age ranges exhibit grain ages that extend above and below the range of interpolated bedrock ages, especially in the modern river samples. For example, in sample 17PG29s, 10 out of 102 grain ages are older than ~21 Ma (Table S9 in Falkowski et al. [2021]) and would have to be removed from the age distribution according to the bedrock age map of the entire catchment (black outline in Figure 1c). In addition, removal of a total of 20 grain ages (three younger than ~3.5 Ma and 17 older than ~12.6 Ma; Table S9 in Falkowski et al. [2021]) is needed when considering that the Leones and Fiero lakes trap all modern sediments of sand and coarser size. These sediment traps would prevent the high-elevation western part of the catchment providing sediment to the rivers (gray dashed outline in Figure 1c). In contrast, sample 17PG30p only yields one grain age (~22.9 Ma; Table S10 in Falkowski et al. [2021]) that would have to be excluded when considering the entire catchment, and seven grain ages (two younger than ~3.4 Ma and five older than ~12.8 Ma; Table S10 in Falkowski et al. [2021]) when considering only the eastern part of the catchment as a sediment source. See Section 5.3.3 for an illustration of this.

There are two possible explanations for detrital ages that are either younger or older than predicted. The first is that the age-elevation relationship is not applicable over the eastern part of the catchment. Only bedrock from the western part of the catchment was sampled, due to accessibility in the field. Insufficient ZHe data exist from the Northern Patagonian Icefield and high elevations to quantify spatial changes in the age-elevation relationship in the study area. However, there are some indications that ZHe ages might increase eastward from the highest topography along the Leones Valley. An across-strike, horizontal profile ~25 km to the north shows older ZHe ages from similar elevations (<500 m) than in the Leones Valley but ages increase east- and westward from the crest of the Patagonian Andes (Andrić-Tomašević et al., 2021). This is also observed in the south (~51°S; Fosdick et al., 2013) and known from other thermochronometer systems (e.g., Thomson et al., 2010). With regard to the age-elevation relationship, it is also possible that it contains a break in slope at or above the highest-elevation bedrock sample (see 2,325 m contour in Figure 1c) and that higher-elevation rocks have much older ZHe ages. We consider this as unlikely due to the maximum catchment elevation of 3,630 m (Table 1) and the relatively young zircon fission track ages of two of the samples (~6 Ma and ~14.5 Ma; Figure 3a; Andrić-Tomašević et al., 2021). Furthermore, due to the sediment traps (lakes) the likely source elevations in the eastern part of the catchment are lower (maximum of 2,245 m; Table 1) than the highest bedrock sample.

The second possible explanation for detrital ages that are either younger or older than the bedrock age map is that those ages are "erroneously" young or old due to potential thermochronology technique complications. Ages that are younger than predicted can result from zonation of uranium and thorium within a mineral grain, specifically uranium/thorium-rich grain rims. In that case, the alpha-ejection correction underestimates non-diffusional helium loss (Farley et al., 1996). The distributions of induced tracks in the two available zircon fission track mounts do not indicate that zoning of uranium is a problem in zircons from the Cretaceous batholith (Figure 1d). More specifically, only ~3% of mounted grains show limited zoning with uranium-rich spots at zircon rims. However, this could be different in other parts of the study area. Furthermore, a small grain size can influence a thermochronometric age (Farley et al., 1996). We picked grains of >60 μm diameter and plots of ZHe age against grain size do not show a systematic trend

of the youngest grains being the smallest (Figure S3 in Supporting Information S1). Fractures in grains could cause helium loss and yield erroneously young ages. However, due to the quality of zircons in all samples, we did not select fractured grains. Finally, a high amount of radiation damage can result in crystal defects that connect and create pathways for easy helium diffusion, yielding "erroneously" young ZHe ages. Effective uranium (eU) is a proxy for radiation damage (Shuster et al., 2006) and plotted against ZHe age in Figure S3 in Supporting Information S1. We do not observe systematic trends of youngest grains having the highest eU values. Radiation damage can also cause older than expected ZHe ages. A lower amount of accumulated radiation damage may cause crystal defects that are not connected and result in enhanced retention of helium (Guenthner et al., 2013). However, we do not observe a trend of oldest grain ages having higher eU values (Figure S3 in Supporting Information S1). Other reasons why grains might be "erroneously" old include uranium/thorium-rich grain cores, and mineral or fluid inclusions that contribute helium. While we cannot exclude the effect of inclusions in measured zircons, the effect of added helium from inclusions is generally small due to the relatively high concentration of uranium and thorium, and therefore helium, in zircons. All measured zircons contained inclusions, including the zircons from bedrock samples. In both cases, zircons with the smallest and fewest inclusions were picked for measurements.

Based on the above discussion, we conclude that the "too young" and "too old" ages result from a combination of tectonic and technical factors. It is unlikely that all detrital ages that are older than predicted are "erroneously" old based on the low amount of old outliers in the granitoid bedrock samples (<3%; Section 3.1) and the likely eastward increase in ZHe ages that would shift the age-elevation relationship to older ages, even over the length scale of ~20 km. At the same time, we consider it unlikely that the entire detrital age range up to ~109 Ma (Tables S5–S10 in Falkowski et al. [2021]) reflects bedrock ages in the study area. This assumption is mainly based on the detrital age range we find in the easternmost part of the study area that is ~3.5–45 Ma with the majority of ages ~3.5–17 Ma (17PG28s; Figure 1c, Table S8 in Falkowski et al. [2021]). Further support comes from ZHe bedrock ages ~25 km farther north, which are not older than ~60 Ma at the same longitude (Andrić-Tomašević et al., 2021). The few young ages (<2 Ma; Tables S5–S10 in Falkowski et al. [2021]) observed might be "erroneously" young as we do not expect sediments to be sourced from correspondingly low elevations (hundreds of meters below sea level, if the linear age-elevation relationship would simply be extrapolated; see Section 5.2).

Based on the above, we refrain from either estimating eastward changes in the bedrock age-elevation relationship or simply assuming that ZHe ages that are older than predicted are "erroneously" old. To do so would result in more uncertainties than necessary in our analysis. Instead, the bedrock age-elevation relationship is considered valid for the western part of the catchment and used in the following analysis of upstream glacial erosion for the moraine sample (Section 5.2). However, an analysis of erosion patterns of the modern trunk river samples may not yield reliable results and we cautiously limit our analysis to downstream variations in the age distributions of the sand (Section 5.3.1) and pebble (Section 5.3.2) samples. The river samples are also used for comparison of age distributions between different grain sizes (Section 5.3.3). We note that our analysis of river samples from the eastern part of the catchment uses the detrital age uncertainty estimate derived from the reproducibility of available bedrock samples from the western study area. The true uncertainty of the eastern samples could potentially be larger (or smaller) in the east, where lithologies are different (Figure 1d). However, the age uncertainty chosen is rather conservative. Therefore, we do not expect a change in our overall results for the comparisons of modern river age distributions.

5.2. Upstream Glacial Erosion Distribution From the Moraine Sample

Analysis of the elevation distribution of glacial erosion from the ~2.5–1.1 ka moraine sample was conducted by clipping the detrital age population by five grains according to the bedrock age map and associated uncertainties. Grains removed from the analysis include two at ~1 Ma, and three with ages of ~17–23 Ma (Table S5 in Falkowski et al. [2021]). Figures 5a and 5b show the observed and predicted KDEs and CADs. Predicted age distributions are derived from a spatially uniform erosion scenario (purple curves), a slope-dependent erosion scenario (erosional weights are proportional to slope; black curves) and a best-fit erosion scenario (red curves; cf., Section 3.2.2). The resulting best-fit normalized erosion probability with 95% confidence envelope is plotted against elevation in Figure 5b and the best-fit erosion scenario is shown in map view in Figure 5d.

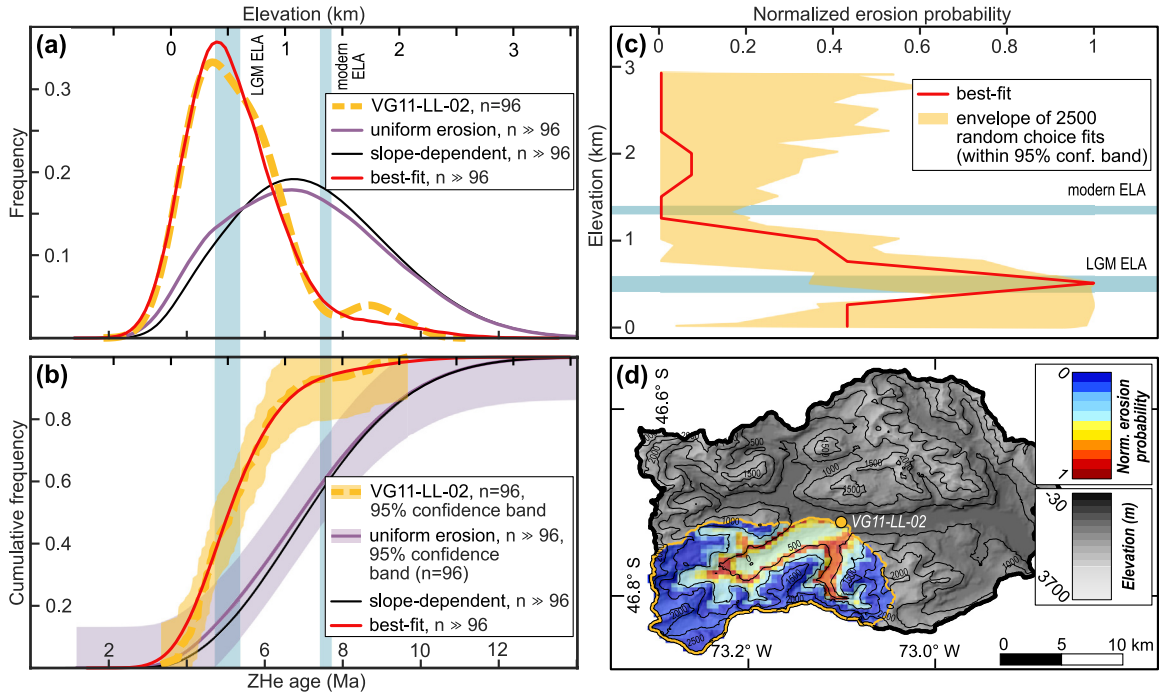

Figure 5. Observed and predicted age distributions, and the elevation distribution of erosion for the ~2.5–1.1 ka moraine sample VG11-LL-02. (a) Kernel density estimation (KDE) of observed (yellow dashed curve) and predicted (black, purple, red curves) age distributions. Bottom *x*-axis is zircon (U-Th)/He (ZHe) age and top *x*-axis is elevation based on the age-elevation relationship (Figure 3a). (b) Cumulative age distributions (CADs) for the same scenarios as in (a). (c) Normalized erosion probability per 250 m elevation sectors. (d) Map view of best-fit normalized (norm.) erosion probability. (a–c) Blue bands represent the locations of the modern and Last Glacial Maximum (LGM) equilibrium line altitudes (ELA).

The uniform and slope-dependent erosion scenarios predict very similar age distributions for the moraine sample location. In comparison, the observed age distribution is narrower and shifted considerably to younger ages than the predicted distributions (Figures 5a and 5b). The best-fit erosion scenario indicates that the majority of the moraine sediment was sourced from elevations below ~1,000 m with a distinct peak at ~500 m or lower (yellow envelope in Figure 5c). This peak coincides with the position of the LGM ELA (at ~400–600 m; Hubbard et al., 2005), assuming that the neoglacial ELA during moraine deposition was higher than the LGM ELA.

Furthermore, the analysis shows a significant contribution of sediment sourced from the lowest elevation sector that is now occupied by Lago Leones (~0–300 m), but not from elevations below sea level. More specifically, only two "too young" grain ages that would suggest source elevations below sea level were clipped/removed from the analysis (1.1 ± 0.2 Ma and 1.4 ± 0.2 Ma; Table S5 in Falkowski et al. [2021]). This suggests that this part of the valley was overdeepened before deposition of the moraine and that not much, if any, of the sedimentary infill from <0 m was recycled and deposited within the moraine.

The two youngest ages that were removed are likely "erroneously" young (Section 5.1) and not from recycled material eroded from depths representative of overdeepening. If the age-elevation relationship was extrapolated to elevations below sea level, the two young ages would suggest source elevations of at least −550 m and up to −1,100 m, including uncertainties. While the sediment infill in the valley could conceivably be ~1,000 m (for example, overdeepenings in the European Alps can be up to 1,000 m deep; Preusser et al., 2010), we consider this as unlikely. Most other detrital samples also do not suggest input from elevations below sea level (or "erroneously" young ages), with the exception of the pebble sample 17PG27p (Table S7 in Falkowski et al. [2021]).

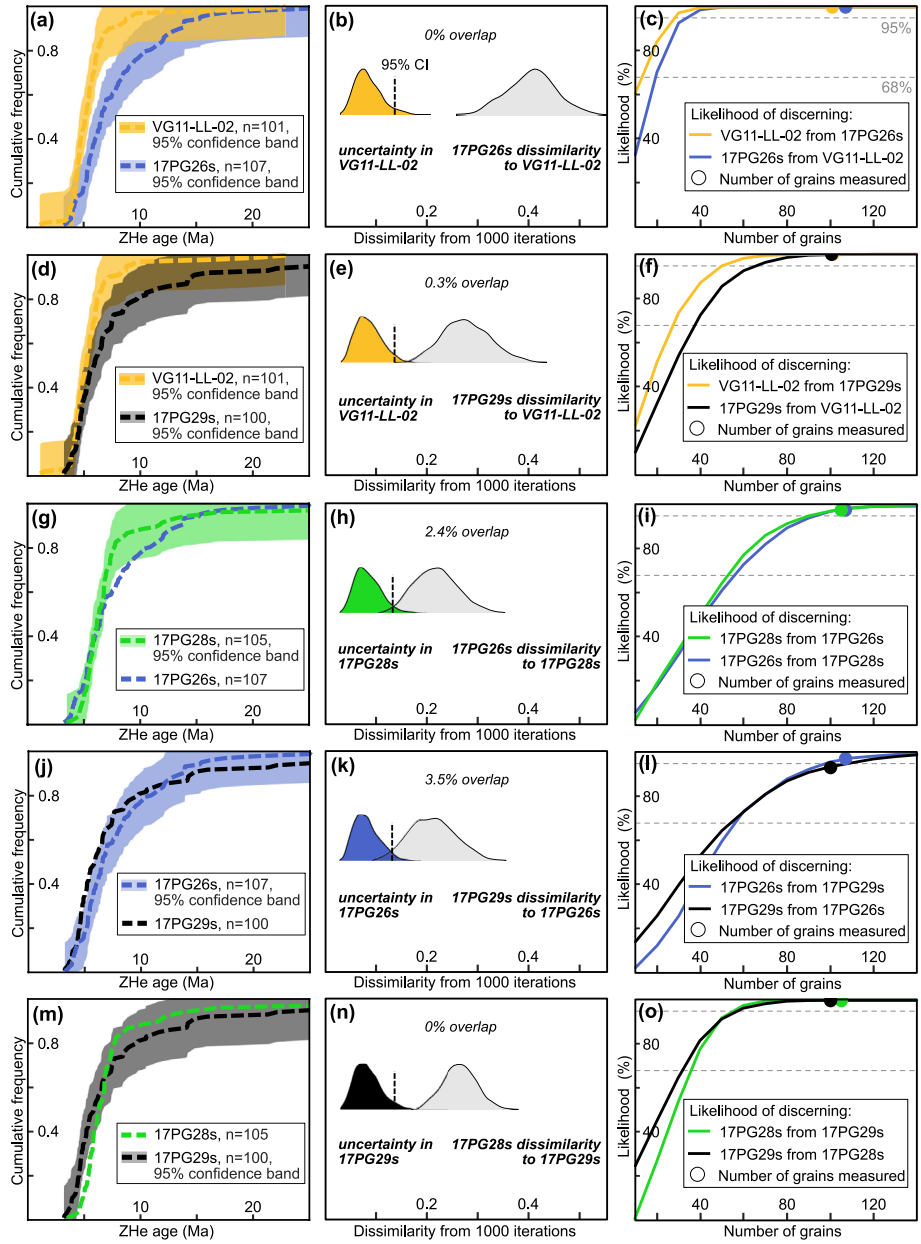

Figure 6. Comparison of the zircon (U-Th)/He (ZHe) age distributions of moraine and modern sand samples. (a, d, g, j, m) Cumulative age distributions (CADs) of compared sample pairs. The age axes are clipped at 25 Ma. (b, e, h, k, n) Probability distributions of dissimilarities between two samples (right curve) and of dissimilarities within one sample (i.e., its uncertainty; left curve). The dashed line marks the one-sided 95% confidence interval (CI) of the latter. The percentage of "overlap" informs the fraction of the gray area left of the dashed line. (c, f, i, l, o) Likelihood to discern between samples as a function of sample size. See Section 3.2.2 for details of the plots.

5.3. Detrital Age Distributions From the Modern River Samples

5.3.1. Downstream Age Variations in the Sand Fraction

Downstream age variations in the sand fraction were analyzed through comparison of neighboring sand sample pairs separated along the river. As the moraine sample was mostly sand, we include it in this comparison, but note again that it also contained granules and some fine to coarse pebbles. Figure 6 shows three types of plots per sample pair comparison, which all illustrate the dissimilarity between samples, as described in Section 3.2.2.

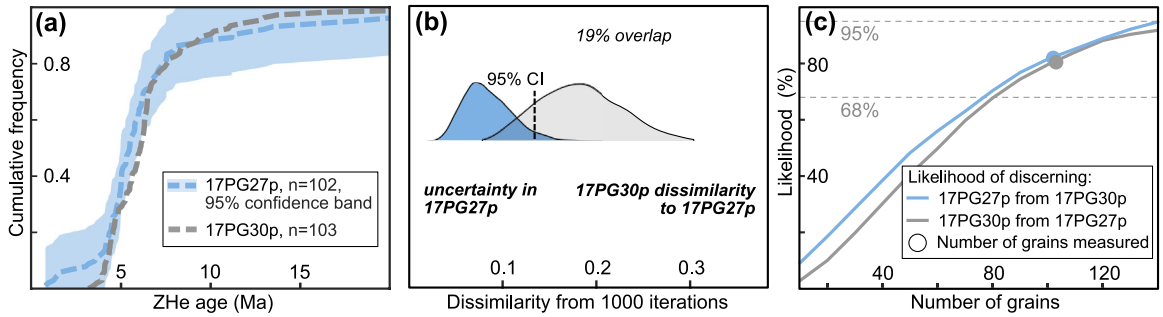

Figure 7. Comparison of the zircon (U-Th)/He (ZHe) age distributions of pebble samples. (a) Cumulative age distributions (CADs) of 17PG27p and 17PG30p. The age axis is clipped at 20 Ma. (b) Probability distributions of dissimilarities between two samples (right curve) and of dissimilarities within one sample (i.e., its uncertainty; left curve). The dashed line marks the one-sided 95% confidence interval (CI) of the latter. The percentage of "overlap" informs the fraction of the gray area left of the dashed line. (c) Likelihood to discern between samples as a function of sample size. See Section 3.2.2 for details of the plots.

The likelihood of discerning between all compared sample pairs varies slightly but is above 95% in all cases. This is the likelihood that the dissimilarity between samples A and B is less or equal to the 95% confidence interval of sample A (dashed vertical lines in Figures 6b, 6e, 6h, 6k, and 6n). For brevity, this likelihood is here referred to as "overlap" (Figure 6). For example, in Figures 6b and 6n the distributions of dissimilarity to sample A both have 0% overlap but plot at different distances from each other. The minimum number of grains necessary to discern between samples with a high likelihood is lower in Figure 6c than in 6o. In Figures 6c, 6f, 6i, 6l, and 6o, we compare sample A to sample B and vice versa, resulting in two curves.

For example, samples VG11-LL-02 (moraine) and 17PG26s (first sample downstream, cf., Figure 1) are most dissimilar to each other (Figures 6a–6c). Their dissimilarity distributions do not overlap (Figure 6b) and indicate that the samples could be discerned from each other with a high likelihood already with <40 grains (Figure 6c). Among the river samples, 17PG26s and 17PG29s (the first two trunk stream sample locations, cf., Figure 1) have the highest amount of overlap with 3.5% (Figure 6k), which reflects a likelihood of discerning between the samples of 96.5% (Figure 6l). For a summary of the dissimilarities among all samples also see the MDS plot in Figure 4c.

In summary, the dissimilarity analysis shows we can distinguish between all sand (and moraine) samples with a very high likelihood. While we are not able to interpret potential differences in the underlying erosion patterns in the respective upstream catchments of the samples, their dissimilarity suggests that part of the sediment source was not the same. This implies the river samples do not reflect recycled material from the upstream moraine and, possibly, related deposits such as sandurs, but are probably sourced by sediments from the eastern part of the Leones catchment with continuous input from tributaries. This is indicated by the observation that the downstream-most sand sample (17PG29s) is discernable from both the upstream trunk stream sample (17PG26s; Figures 6j–6l) and the closer upstream tributary sample (17PG28s; Figures 6m–6o and 1 for sample locations).

5.3.2. Downstream Age Variations in the Pebble Fraction

A comparison between pebble samples 17PG27p and 17PG30p is shown in Figure 7 using the same type of plots as previously discussed for Figure 6. The overlap of 19% between pebble samples (Figure 7b) is much higher in comparison to the sand and moraine samples shown in the previous section. The likelihood of discerning between the samples is accordingly ~80% (Figure 7c). This difference to the downstream sand samples suggests differences in erosion or transport behavior, which is further discussed in Section 6.2.

5.3.3. Comparison of Sand and Pebble Samples From the Same Location

In Figure 8, we present analyses from the modern trunk river samples according to sampling location. Figures 8a–8d show the observed and predicted KDEs and CADs and analyses of dissimilarity for 17PG26s/-27p from ~7.5 km downstream of the sampled moraine, and Figures 8e–8h for 17PG29s/-30p from ~19 km downstream of the sampled moraine.

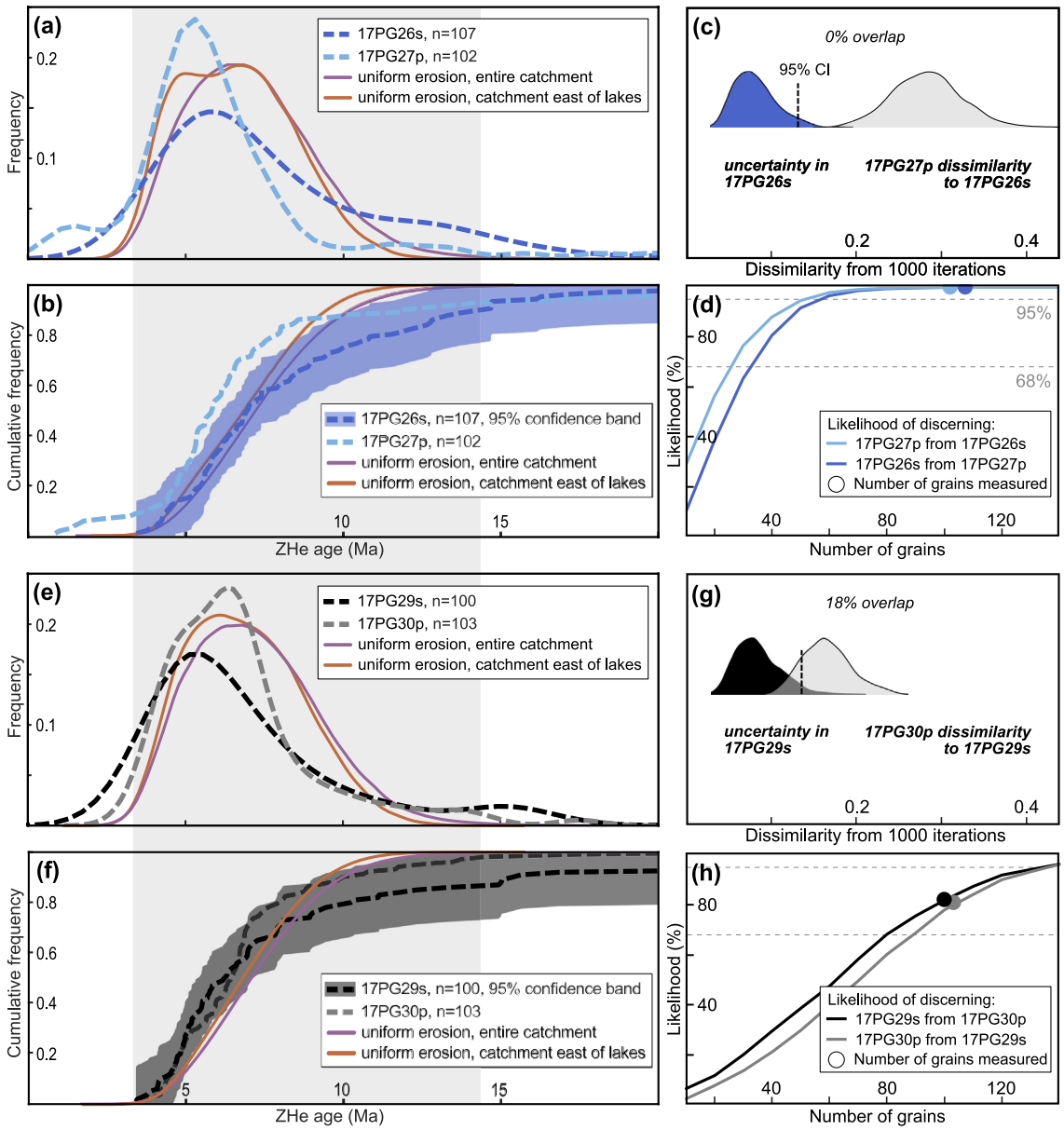

Figure 8. Comparison of the zircon (U-Th)/He (ZHe) age distributions of modern trunk river sand and pebble samples. (a, b, e, and f) Kernel density estimations (KDEs) and cumulative age distributions (CADs) of 17PG26s and 17PG27p (a, b) and 17PG29s and 17PG30p (e, f) from the same sampling location, respectively (Figure 1). The purple and orange curves in (a, b, e, and f) are predicted KDEs and CADs from a uniform erosion scenario (light gray band across left panels) of the entire catchment area upstream of the respective sampling locations and of the catchment area excluding the areas behind Leones and Fiero lakes. These would only be valid, if the bedrock age-elevation relationship holds for the entire catchment area (see Section 5.1 for details). Age axes are clipped at 20 Ma. (c and g) Probability distributions of dissimilarities between two samples (right curve) and of dissimilarities within one sample (i.e., its uncertainty; left curve). The dashed line marks the one-sided 95% confidence interval (CI) of the latter. The percentage of "overlap" informs the fraction of the gray area left of the dashed line. (d and h) Likelihood to discern between samples as a function of sample size. See Section 3.2.2 for details of the plots.

Predicted age distributions are based on hypothetical uniform erosion scenarios for two cases, including erosion over the entire upstream catchment (purple curves in Figures 8a, 8b, 8e, and 8f) and over the upstream catchment excluding the area upstream of Leones and Fiero lakes (orange curves in Figures 8a, 8b, 8e, and 8f). Both cases assume that the age-elevation relationship was valid in the eastern half of the catchment. Results illustrate that up to 25% of grain ages are older than the maximum predicted age range. If sediment was only derived from the catchment in front of the lakes, where the elevation range is lower (Table 1), even more grain ages would be older than predicted, as described in Section 5.1.

More importantly here is the comparison between observed age distributions and the variations in ZHe ages with grain size fraction. Age distributions from sand and pebbles at the upstream-most location show 0% overlap (Figure 8c) and hence a 100% likelihood of discerning between the two grain size fractions (Figure 8d). At the downstream-most location, the CAD of the sand sample lies completely within the confidence band of the pebble CAD, and vice versa (Figure 8f). The likelihood to discern between sand and pebble age distributions is ~80% (Figure 8h). The difference in dissimilarities between 17PG26s/-27p and 17PG29s/-30p is also well documented in the MDS plot (Figure 4c), where they do not overlap and overlap, respectively.

Assuming that sand and pebble fractions from one location represent the same upstream catchment area and time span over which erosion and transport occurred (10^1–10^2 years), and that not much glacial sediments are recycled, then the differences in grain size fractions can be interpreted in terms of sediment production patterns. Why these might vary between sand and pebbles and between downstream locations is discussed in Section 6.3.

6. Discussion

In this section, we present a synthesis of observations and discuss our interpretations with respect to the three hypotheses stated in Section 1.

6.1. Evaluation of Glacial Erosion Pattern With Respect to the ELA (Hypothesis 1)

6.1.1. Leones Glacier Catchment

Results from the ~2.5–1.1 ka Lago Leones moraine provide a snapshot of the pattern of glacial erosion during neoglacial ice readvances, when the Leones Glacier was 10 km longer than at present (Section 2.1). The data do not resolve temporal changes in the erosion pattern but allow some inferences with respect to the LGM. For a longer-term (10^6 years) and valley-scale perspective on glacial erosion and related exhumation in the Leones Valley, the reader is referred to Andrić-Tomašević et al. (2021).

We found that the vast majority of analyzed grains (>80%) deposited within the moraine were sourced from elevations between ~1,000 and ~0 m with a peak in erosion probability at ~500 m (vertical resolution of 250 m; Figure 5, Section 5.2). This elevation range corresponds to the position of previous ELAs, with the LGM ELA at ~400–600 m (Hubbard et al., 2005) and the ELA during deposition of the moraine likely between the modern (~1,350 m; Rivera et al., 2007) and the LGM ELA. We interpret the results as limited erosion in the accumulation area of the glacier and focused erosion below the neoglacial ELA and at the LGM ELA, where glacial sliding velocities were likely highest. Alternative explanations for why almost no analyzed grains were sourced from >1,000 m include storage of those sediments within depressions beneath the glacier, and variations in zircon fertility, that is, low fertility at high elevations. However, it is unlikely that all sediments from high elevations from across all glacier tributaries were stored and not deposited in the moraine. Due to good bedrock control in cooling ages in this part of the catchment we can rule out low zircon fertility at high elevations.

The erosional pattern observed is indicative of an increase in topographic relief by incising the valley and limited erosion at higher elevations (above glacial/neoglacial ELAs). Thomson et al. (2010) suggested for the Southern Patagonian Andes that glaciers were cold-based and therefore protect the mountain range from erosion (based on low-temperature thermochronometry and meridional topographic variations), while Herman and Brandon (2015) concluded from a glacial erosion model that wet-based conditions prevailed even during glacial maxima with the possible exception of the highest elevations where ice is thin. Based on this, it is unlikely that the Leones Glacier was cold-based already at elevations of 1,000 m and above and wet-based below, but rather that it was wet-based during the neoglacial and that ice sliding velocities and pre-existing topography might be the controlling factors for the observed erosion pattern.

Under the assumption that the elevation difference between LGM and neoglacial ELAs is higher than the vertical resolution in the elevation distribution of erosion, the peak in erosion probability at the LGM ELA needs explanation. Pre-existing topography might have played an important role, where past glacial erosion produced steeper bedrock slopes at the glacial ELA and below. This could have increased ice sliding

velocities and further focused erosion at low elevations during neoglacial ice advance in combination with a lowered ELA (presumably below 1,000 m). An ice cliff at ~750 m elevation in the catchment might reflect this (Section 2.1, Figure S2 in Supporting Information S1). An alternative explanation could be that sediments deposited in the Lago Leones moraine were recycled material from much earlier erosion and that the signal actually reflects the LGM erosion pattern. Moraine material would have been stored within the space now filled by the lake and exarated during the neoglacial ice advance. This cannot be ruled out as we cannot easily study the LGM erosion pattern by the Leones Glacier. Glacial deposits from the LGM were deposited >150 km to the east and reflect a significantly different (larger) catchment (Figure 1a). However, the valley where Lago Leones is located was overdeepened before deposition of the moraine, possibly during the LGM and earlier ice advances (Section 5.2). This could indicate that the erosion pattern during the LGM was shifted to lower elevations than what is observed from our observations from the Lago Leones moraine and erosion was focused below the LGM ELA. In short, timing of erosion of the Lago Leones moraine material is uncertain to some degree, but with the current data, we assume that while some sediment was probably recycled, the majority of material analyzed was eroded during the neoglacial period.

Our inferences of glacial erosion patterns corroborate previous work indicating that glacial erosion rates increase (nonlinearly) with ice sliding velocity (e.g., Herman et al., 2015; Humphrey & Raymond, 1994; Koppes et al., 2015; Yanites & Ehlers, 2016). Where sliding velocities of temperate glaciers are highest changes over glacial cycles or even on syn-glacial timescale (e.g., Herman & Braun, 2008; Yanites & Ehlers, 2016). Several factors influence the evolution of glacial erosion patterns, such as the position of the long-term ELA, the form of the pre-existing landscape, frequency and amplitude of climatic oscillations driving glaciation, local climate conditions (temperature and precipitation), and tectonic rock uplift rates (e.g., Herman & Braun, 2008; Sternai et al., 2013; Yanites & Ehlers, 2012, 2016). Glacial erosion patterns have also been found to depend on the spatial and temporal scales considered. For example, the glacial buzzsaw hypothesis predicts efficient erosion at and above the ELA to shift the hypsometric maximum to just below the ELA, hence limiting the mean height of mountain ranges (Brozović et al., 1997; Egholm et al., 2009). Observations that deep incision of trunk valleys at elevations below the glacial ELA, as for example seen in the Leones Valley, can increase topographic relief and isostatically uplift rocks (e.g., in the European Alps; Valla et al., 2011) does not contradict the buzzsaw hypothesis. Egholm et al. (2009) demonstrated the influence of topography on ice flow and glacial erosion efficiency, such that trunk valley glaciers and different sizes of tributary glaciers shape the landscape differently, including deep incision below the ELA while the regional character of the landscape may exhibit a buzzsaw signal. Based on models for the European Alps, Sternai et al. (2013) argued that glacial erosion is more complex than a decrease or increase in relief but evolves through time and space with headward propagation of glacial erosion. They suggested that glacial erosion is focused at lower reaches (below the ELA) in the early stages of glaciation and at higher elevations in the later stages, when the steepened slopes move headward. Bedrock AHe thermochronometric data integrated with a thermokinematic model (Southern Alps, New Zealand; Shuster et al., 2011) or with a glacial surface process model (Coast Mountains, Canada; Yanites & Ehlers, 2016) also suggest spatially and temporally highly variable glacial erosion rates that are dependent on ice sliding velocities and that an orogen-scale reduction in relief occurs, while, locally, relief increases due to headward propagation of glacial erosion.

Independent of some uncertainty in the timing of erosion of material deposited in the moraine, our results support the hypothesis that the position of the ELA influences the distribution of erosion in a glacial catchment. Steepened slopes created during glacial maxima may further influence the spatial erosion pattern during subsequent glacial advances in combination with a lowered ELA. Slope-dependency of erosion alone could not explain the erosion pattern (Figure 5). It is important to note that the observed erosion pattern is based on the analyzed grain size fractions in the moraine sample and we suggest that the material was dominantly produced by glacial abrasion. Larger grain size fractions might be produced by glacial quarrying, which is more strongly influenced by effective hydrostatic pressure at the bed (e.g., Hallet, 1979, 1996; Ugelvig & Egholm, 2018; Ugelvig et al., 2016). Future studies on erosion patterns in glacial catchments could include systematic investigations of separately processed and more different grain size fractions from moraines to evaluate if different glacial erosion processes (quarrying vs. abrasion) are reflected in grain age distributions. The importance of grain size variations in ages has been demonstrated for modern fluvial and alluvial settings (e.g., Lukens et al., 2016, 2020; Riebe et al., 2015; Vermeesch, 2007) and is suggested by our comparison of modern sand and pebble samples as well (Section 6.3).

6.1.2. Comparison to Previous Tracer Studies

Previous studies have investigated glacial deposits or direct outwash from modern alpine glaciers to reconstruct patterns of glacial erosion. In this section, we point out some similarities and differences to results presented here. However, we note that a direct comparison to our results from the ∼200 km^2 Lago Leones moraine upstream catchment (46.7°S), that is underlain by Cretaceous granitoids, is complicated by differences in catchment size, lithology, material properties such as fracture density, geomorphology, ice extents, tectonic uplift, climate, and sampling strategies.

Examples of lessons learned from related studies are as follows. Tranel et al. (2011) used AHe tracer thermochronology in the Teton Range, USA (43.7°N), to study sand-sized material from a ∼14 ka moraine in a ∼8 km^2 catchment with steep slopes underlain by fractured Proterozoic gneiss and monzonite. Elevations range in the Teton catchment from ∼2,200–4,200 m with the LGM ELA at ∼2,600 m. Tranel et al. (2011) did not observe such a proportionally large sediment input from elevations around the glacial ELA as in this study.

Ehlers et al. (2015) applied tracer AHe thermochronology to determine the erosion pattern in the Tiedemann Glacier catchment of the Coast Mountains, Canada (51.3°N). They sampled modern outwash sand close to the modern glacier terminus. The ∼130 km^2 catchment is at elevations of 530–3,960 m and underlain by Early Tertiary granitoids. Ehlers et al. (2015) determined that the largest sediment input was derived from elevations around the present-day ELA (∼2,700–2,900 m), but did not find a pattern as observed from our moraine sample with very limited erosion at higher elevations within the catchment. Enkelmann and Ehlers (2015) showed for the same catchment based on apatite fission track age distributions from modern outwash and moraines of different ages (present-day, 1600 CE, and 2900 BCE) that the erosion patterns changed over time, but did not provide an analysis of elevation distribution of erosion. Due to the geomorphology of the Leones Valley (i.e., lakes trapping material eroded by glaciers today) and uncertain bedrock age-elevation relationship we can unfortunately not compare between modern and past erosion patterns. This could be addressed through future sampling campaigns with detrital samples from west and north of the lakes (cf., Figure 1) and bedrock samples from the eastern part of the catchment.

Finally, Jiao et al. (2018) used Raman spectroscopy of carbonaceous material from a sediment core offshore of the Southern Alps, New Zealand (44°S). The catchment area encompassed several glacial catchments (catchment area of ∼130 × 30 km) where the elevation distribution of erosion was traceable due to a spatial gradient in the metamorphic grade of exposed schist. The results of this study suggest enhanced glacial erosion in the lower reaches of the glacial catchments during the LGM, and focusing of fluvial erosion and mass wasting processes within the upper reaches of catchments during the Holocene. This change in the focus of erosion corresponds with elevations at and below the LGM and modern ELAs (∼500–700 m and ∼1,000 m higher, respectively). At least for the glacial erosion signal, we can compare this focused erosion at the ELA during glacial episodes to our study, although our results reflect one glacial catchment and Jiao et al.'s (2018) samples reflect an integrated signal from a large catchment area and over different timespans.

In summary, this study and previous studies highlight the potential of tracer applications to investigate glacial erosion over different spatial and temporal scales. Results suggest the importance of the position of the glacial and interglacial ELA to focus erosion (this study; Ehlers et al., 2015; Jiao et al., 2018), and particularly of the glacial ELA with significantly enhanced erosion at and below this zone (this study; Jiao et al., 2018). Furthermore, erosion patterns may change rapidly, also on syn- or post-glacial timescales (Enkelmann & Ehlers, 2015). Investigating well-dated deposits with tracer techniques can capture these signals, if the catchment area does not change over time or changes are known (Enkelmann & Ehlers, 2015; Jiao et al., 2018). However, the above list of studies also shows inconclusive aspects of observational studies. For example, in the Teton catchment no significant influence of the glacial ELA on the erosion pattern was reported (Tranel et al., 2011). It is unclear how the factors listed at the beginning of this section (catchment size, morphology, material properties, etc.) influence the comparison between glacial erosion patterns of different study areas. More observational data are needed to better understand broader trends and specific differences between settings.

6.2. Evaluation of Downstream Variations in Age Distributions (Hypothesis 2)

Here, we discuss variations in downstream age distributions observed in sand and pebble samples from the modern river channel. Sand and pebble samples from the trunk stream were collected ~11 km apart and a sand sample from a tributary was collected approximately midway between the trunk sampling locations (Figures 1 and 4). We showed that all ZHe age distributions from sand fractions are distinguishable from each other and from the moraine sample, while the two pebble fractions cannot be discerned with the same high likelihood (Sections 5.3.1 and 5.3.2, Figures 6 and 7). Variations in the age distributions could indicate either partly different source areas or sediment mixing processes during transport. The difference between dissimilarities among sand samples and pebble samples hints to different erosion and transport behavior of different grain size fractions. At the moment, there are too many unknowns to evaluate this result more rigorously. For example, in addition to the likely eastward change in the bedrock age-elevation relationship, there can be changes in the erosion pattern, different amounts of sediment recycling, or differences in how sand and pebbles are produced from the different lithologies (granitoids and metasediments). Finally, future studies could also consider if variations in modern vegetation cover could influence glacial catchments, as has been recently documented for other (non-glacial) settings in South America (Starke et al., 2020). All of these factors may contribute to the shape of downstream-directed detrital age distributions.

A few additional items can be learned from the observations with regard to sediment sources and sampling. For example, we find that modern river sand samples do not contain a constitutive portion of recycled material from the upstream neoglacial moraine or sandur, that is, upper layer of the valley infill that was deposited when the Leones Glacier terminated at the end of the present lake (Harrison et al., 2008). This may be due to a number of factors including: (a) the age of the moraine or high discharge and precipitation, such that the loose fractions have been washed out before, or (b) that sediment input from downstream of the moraine is proportionally higher, or a combination of the above. Sediments are not derived from the western part of the catchment upstream of the Leones and Fiero lakes. Instead, the modern river channel is sourced from the eastern part of the Leones catchment with a continuous input from the valley walls along the Leones River and tributaries as indicated by the downstream variation in age distributions from trunk and tributary. This is supported by the evolution of lithology abundances in the pebble fractions in comparison to the geologic map (cf., Figures 1d and 2a and Section 2.2). Mostly granitoid rocks are exposed in the western and central part of the study area, while the easternmost part is dominated by metamorphic and volcanic rocks. The western of the two trunk stream samples had 27% metamorphic and volcanic (and unidentified) pebbles, while the eastern sampling location had 45% of those lithologies (Figure 2a). Sediment input from the tributaries comprises modern sediment production over presumably 10^1–10^2 years time scales. Tributary catchments reach elevations up to ~2,250 m and drain into the Leones Valley from the north and south (Figure 1, Table 1). All tributary catchments today still have glaciers in their higher reaches with termini at >700 m and small (in comparison to Lago Leones) proglacial lakes dammed by LIA moraines (cf., Section 2.1 and Figure 1b). Due to the uncertainties in the bedrock age-elevation relationship, it is unknown whether the samples were sourced over the entire elevation range. If the age-elevation relationship was valid for the eastern part of the catchment, the tributary sand sample would indicate that all elevations from at least the tributary in the southeast contributed sediments (as uniform-erosion predicted and observed age distributions cannot be discerned; Text S1, Figure S4 in Supporting Information S1). With a likely shift to older bedrock ages in that part of the catchment however, sediments would appear preferentially sourced from medium and lower elevations (Figure S4 in Supporting Information S1). In addition to the source of modern sediments (including LIA sediments), sediments that were eroded over the entire catchment during neoglacial time, and possibly earlier, might be recycled by modern fluvial and hillslope processes.

Independent of our inability to robustly interpret variations observed in downstream sand age distributions (which are less pronounced in the pebble fraction), these variations present caveats and opportunities. More specifically, these results highlight the need to carefully consider sampling locations when characterizing erosion patterns or exhumation in larger glacial catchments with several tributaries. In particular, for large catchments with multiple tributaries it is essential to have a dense bedrock age-elevation sample suite to evaluate systematic changes in the observed detrital age distributions. But results also show that large

moraines within catchments do not necessarily dominate age distributions in modern downstream river samples.

Regarding hypothesis 2 that changes in surface and/or tectonic processes along the length scale of a valley should be reflected in downstream age variations, we find this is difficult to fully evaluate from our results alone. Ultimately, testing this hypothesis depends on the magnitude of change and factors that influence the capability of detecting this at a high level of confidence, such as the age range in the age-elevation relationship and age uncertainty.

6.3. Evaluation of Grain Size Differences and Erosion Mechanisms (Hypothesis 3)

The comparison of different grain sizes from the same sampling location showed that sand and pebble age distributions in samples 17PG26s and 17PG27p can be discerned with a high likelihood. This result indicates they have different source elevation regions. In contrast, the likelihood to discern between samples 17PG29s and 17PG30p is smaller and they might represent more similar, or the same, source elevation regions (Section 5.3.3, Figure 8). From the comparison between moraine and modern river age distributions it appears that reworking of glacial sediment from the moraine is not dominant for the sand fraction (cf., Section 5.3.1), but future studies are needed to confirm this assumption for the pebble age distributions by sampling and analyzing separately the coarser size fraction in the moraine. For now, we assume that recycling of glacial deposits is not dominant and that sand and pebbles from the same location represent the same upstream catchment area. Even though we refrain from relating detrital ages to specific source elevations for the modern trunk river samples, they can qualitatively be compared to each other to identify preferential source elevations of the sand and pebble fractions (lower/higher in the catchment, or lower/higher in relation to the other grain size fraction).

The upstream catchment for the samples 17PG26s/-27p encompasses an area of ~94 km^2 and an elevation range of ~235–2,047 m, when excluding the area west of the lakes (Table 1). The pebble age distribution is narrower/steeper than the sand age distribution and shows that pebbles were preferentially sourced from a smaller elevation range than the sand fraction (in the KDE/CAD, respectively; Figures 4, 8a, and 8b). Furthermore, our results indicate the pebbles were preferentially sourced from lower elevations compared to the sand sample (Figures 8a and 8b). The most likely explanation for this relates to differences in the erosion mechanisms at different elevation sectors such that different grain sizes are produced. We hypothesized that a difference in the age distributions in different grain sizes might be related to glacial quarrying (producing larger grain sizes such as pebbles) and abrasion (producing smaller grain sizes such as sand and smaller). In that case, sand might be preferentially produced at lower elevations than pebbles, when coarser sediment is incorporated in the basal ice and enhances abrasion. This pattern is not observed in our samples for the two different grain sizes analyzed. Thus, the spatial distribution of quarrying and abrasion mechanisms might not simply be elevation dependent, or is undetectable from our approach. It is possible that sand is produced over most of the elevation range of the catchment, including higher elevations to where glaciers east of Lago Leones have retreated to (mainly >1,000 m; Figures 1b and 1d), and that pebbles are produced at lower elevations due to rock falls and other mass movements at glacially formed, steep walls of the main valley. Alternatively, the differences in the sand and pebble age distributions could be due to the effect of comminution, where pebbles might be produced in the same proportion at higher elevations but were abraded to sand size during transport (e.g., Dingle et al., 2017). However, due to the fact that this difference is not observed from the location farther downstream, we suggest that comminution likely has an effect but is not the main controlling factor here.

The upstream catchment for the downstream-most river sample location is ~350 km^2 and encompasses elevations between ~235 and 2,245 m (Table 1; gray dashed outline in Figure 1c). In contrast to samples 17PG26s/-27p, our analysis indicates that samples 17PG29s/-30p were sourced from roughly the same proportions of elevations, or that we cannot resolve differences with high confidence. This difference between sample locations is independent of potential changes in the bedrock age-elevation relationship and mixing of modern and stored sediments, as we assume that the latter would be similar for both locations. In combination with the interpretation of continued sediment input from tributaries over the length of the valley (Section 6.2), this indicates that the pattern of sediment production with regard to grain size changes from west to east. This may be the result of the size and geomorphology of the tributaries. The upstream

tributaries sourcing 17PG26s/-27p are smaller and steeper in comparison to the easternmost tributaries that contribute sediments to 17PG29s/-30p (Figure 1). The larger and wider tributaries in the east also contain more extensive present-day ice masses in comparison with the steeper valley walls flanking the Leones Valley at the location of 17PG26s/-27p. The change in proportions of lithology in the easternmost part of the catchment introduces some additional complications due to possible differences in material properties of granitoids and metasediments, such as hardness or grain size that can lead to a variable tendency to produce one grain size fraction or durability during transport. We cannot quantify these potential effects with available data, but mention them for the benefit of future studies. However, at this point, we do not consider the different lithologies as an important factor in our qualitative interpretation for two reasons. Those are the fact that lithology does not change with elevation but from west to east and the fact that the proportion of metasedimentary pebbles present at sample locations varies with the geology in the respective catchment.

Finally, we found that better bedrock age constraints are needed from the eastern part of the study area, as well as coarser grain size samples from the eastern tributaries to fully evaluate hypothesis 3. The qualitative evaluation presented here suggests differences in age distributions for different grain size fractions at one location. This might relate to spatial variations in erosion mechanisms, which depend on erosion agents and geomorphic characteristics that could produce preferentially one grain size. This is not observed at the other location, suggesting variations in catchment erosion mechanisms or patterns over scales of tens of kilometers in the Leones catchment. Important differences can be revealed in the comparison of downstream and same-site grain size fractions.

7. Conclusions

This study investigated both the potential, and limitations, of tracer thermochronology for quantifying glacial erosion and sediment production processes in a tectonically active region with superposed glacial and interglacial episodes. More specifically, we found that the application of detrital ZHe tracer thermochronology in this study demonstrates the utility of this technique for surface processes studies. This higher-temperature technique offers the same potential to address questions of sediment source areas within a catchment as previously shown by lower temperature studies (e.g., AHe). The key in addressing which thermochronometer system is best suited for a particular area depends on prior knowledge of the age-elevation relationship within the catchment—whereby a large range in ages with elevation is preferred for inferring the source elevation from which sediment is derived. This constraint needs to be balanced with the reproducibility of grain ages for the selected thermochronometer system based on bedrock samples.

Second, we successfully demonstrated (as has previous work) that the pattern of glacial erosion can be determined from samples collected from glacigenic sediment. For the Patagonian study area, we find that the maximum in ~2.5–1.1 ka or pre-2.5 ka glacial erosion correlates with elevations near the LGM ELA. This result supports that, at least for the Leones Glacier, the predictions of modeling studies suggesting a maximum in glacial sliding velocities in temperate glaciers occurs near the ELA and that high sliding velocities can result in rapid sustained erosion.

Third, differences in how downstream modern sand and pebble samples compare among each other and how sand and pebble samples from the same site compare to each other suggests that the tracer thermochronology technique is sensitive to possible variations in erosion patterns or mechanisms, or transport mechanisms over short length scales between downstream locations (in our case, ~7–19 km). Detection and interpretation of these changes with a high level of confidence depends on the magnitude of change and the characteristics of the bedrock age-elevation relationship. Furthermore, for large glacial catchments with several tributaries, we recommend sampling different tributaries and locations along the trunk stream, if possible. In addition, the analysis of different grain size fractions within glacigenic sediments (e.g., moraines) in future studies may be able to resolve whether different erosional mechanisms and transport distances influence observed grain-age distributions.

Finally, several notable limitations of the study were identified. Future work could improve upon the approach presented here. First, a bedrock age map must be well established over the entire catchment for the application of tracer thermochronology. Second, the presence of lakes and sediment storage in proglacial river valleys provides both a challenge and opportunity for the technique. The challenge stems from the

setting blocking sediment transport, causing sediment storage for an unknown amount of time, and filtering what material is available for sampling. The opportunity lies in the fact that each of these challenges provides a potential signal that, if accounted for in future sampling approaches, could provide more detailed insight into the dynamics of sediment production, transport, transient storage, and final deposition in glacial valleys.

Data Availability Statement

All data tables associated with this manuscript are archived through the German Research Centre for Geosciences (GeoForschungsZentrum, GFZ) Data Services: Falkowski et al. (2021), https://doi.org/10.5880/fidgeo.2021.027.

Acknowledgments
The study was supported by the German Research Society (DFG) grant EH 329/18-1 to T. A. Ehlers, and STR 373/37-1 to M. R. Strecker. V. Georgieva's co-authorship was supported by the Chilean Government FONDECYT Postdoctoral Grant 2020 Nº 3200375. We thank Leandro Paulino, Juan-Pablo Fuentes Espoz, and the Chilean National Park Authority (CONAF) for support in sample handling within Chile as part of the EarthShape research consortium. We acknowledge detailed and constructive comments by three reviewers, associate editor H. Gray, and editor M. Attal that helped to improve the manuscript. Open access funding enabled and organized by Projekt DEAL.

References

Alley, R. B., Cuffey, K. M., & Zoet, L. K. (2019). Glacial erosion: Status and outlook. *Annals of Glaciology*, *60*(80), 1–13. https://doi.org/10.1017/aog.2019.38

Andrić-Tomašević, N., Falkowski, S., Georgieva, V., Glotzbach, C., Strecker, M. R., & Ehlers, T. A. (2021). Quantifying tectonic and glacial controls on topography in the Patagonian Andes (46.5ºS) from integrated thermochronometry and thermo-kinematic modeling. *Journal of Geophysical Research: Earth Surface*. *126*, e2020JF005993. https://doi.org/10.1029/2020JF005993

Bendick, R., & Ehlers, T. A. (2014). Extreme localized exhumation at syntaxes initiated by subduction geometry. *Geophysical Research Letters*, *41*(16), 5861–5867. https://doi.org/10.1002/2014GL061026

Bernard, M., Steer, P., Gallagher, K., & Egholm, D. L. (2020). Modelling the effects of ice transport and sediment sources on the form of detrital thermochronological age probability distributions from glacial settings. *Earth Surface Dynamics*, *8*(4), 931–953. https://doi.org/10.5194/esurf-8-931-2020

Braun, J., Zwartz, D., & Tomkin, J. H. (1999). A new surface-processes model combining glacial and fluvial erosion. *Annals of Glaciology*, *28*(1), 282–290. https://doi.org/10.3189/172756499781821797

Brewer, I. D., Burbank, D. W., & Hodges, K. V. (2003). Modelling detrital cooling-age populations: Insights from two Himalayan catchments. *Basin Research*, *15*(3), 305–320. https://doi.org/10.1046/j.1365-2117.2003.00211.x

Brozović, N., Burbank, D. W., & Meigs, A. J. (1997). Climatic limits on landscape development in the northwestern Himalaya. *Science*, *276*(5312), 571–574. https://doi.org/10.1126/science.276.5312.571

Caldenius, C. (1932). Las Glaciaciones cuaternarias en la Patagonia y Tierra del Fuego. *Geografiska Annaler*, *14*(1–2), 1–164. https://doi.org/10.1080/20014422.1932.11880545

Carrivick, J. L., Davies, B. J., James, W. H. M., Quincey, D. J., & Glasser, N. F. (2016). Distributed ice thickness and glacier volume in southern South America. *Global and Planetary Change*, *146*, 122–132. https://doi.org/10.1016/j.gloplacha.2016.09.010

Champagnac, J.-D., Valla, P. G., & Herman, F. (2014). Late-Cenozoic relief evolution under evolving climate: A review. *Tectonophysics*, *614*, 44–65. https://doi.org/10.1016/j.tecto.2013.11.037

Chew, D., O'Sullivan, G., Caracciolo, L., Mark, C., & Tyrrell, S. (2020). Sourcing the sand: Accessory mineral fertility, analytical and other biases in detrital U-Pb provenance analysis. *Earth-Science Reviews*, *202*, 103093. https://doi.org/10.1016/j.earscirev.2020.103093

Clapperton, C. M. (1983). The glaciation of the Andes. *Quaternary Science Reviews*, *2*(2–3), 83–84. IN1–IN2, 85–155. https://doi.org/10.1016/0277-3791(83)90005-7

Clapperton, C. M. (1993). Nature of environmental changes in South America at the Last Glacial Maximum. *Palaeogeography, Palaeoclimatology, Palaeoecology*, *101*(3–4), 189–208. https://doi.org/10.1016/0031-0182(93)90012-8

Clinger, A. E., Fox, M., Balco, G., Cuffey, K., & Shuster, D. L. (2020). Detrital thermochronometry reveals that the topography along the Antarctic Peninsula is not a Pleistocene landscape. *Journal of Geophysical Research: Earth Surface*, *125*(6), e2019JF005447. https://doi.org/10.1029/2019JF005447

Davies, B. J., Darvill, C. M., Lovell, H., Bendle, J. M., Dowdeswell, J. A., Fabel, D., et al. (2020). The evolution of the Patagonian Ice Sheet from 35 ka to the present day (PATICE). *Earth-Science Reviews*, *204*, 103152. https://doi.org/10.1016/j.earscirev.2020.103152

Davies, B. J., & Glasser, N. F. (2012). Accelerating shrinkage of Patagonian glaciers from the Little Ice Age (~AD 1870) to 2011. *Journal of Glaciology*, *58*(212), 1063–1084. https://doi.org/10.3189/2012JoG12J026

Dingle, E. H., Attal, M., & Sinclair, H. D. (2017). Abrasion-set limits on Himalayan gravel flux. *Nature*, *544*(7651), 471–474. https://doi.org/10.1038/nature22039

Egholm, D. L., Nielsen, S. B., Pedersen, V. K., & Lesemann, J.-E. (2009). Glacial effects limiting mountain height. *Nature*, *460*(7257), 884–887. https://doi.org/10.1038/nature08263

Egholm, D. L., Pedersen, V. K., Knudsen, M. F., & Larsen, N. K. (2012). Coupling the flow of ice, water, and sediment in a glacial landscape evolution model. *Geomorphology*, *141–142*, 47–66. https://doi.org/10.1016/j.geomorph.2011.12.019

Ehlers, T. A., Szameitat, A., Enkelmann, E., Yanites, B. J., & Woodsworth, G. J. (2015). Identifying spatial variations in glacial catchment erosion with detrital thermochronology. *Journal of Geophysical Research: Earth Surface*, *120*(6), 1023–1039. https://doi.org/10.1002/2014JF003432

Enkelmann, E., & Ehlers, T. A. (2015). Evaluation of detrital thermochronology for quantification of glacial catchment denudation and sediment mixing. *Chemical Geology*, *411*, 299–309. https://doi.org/10.1016/j.chemgeo.2015.07.018

Enkelmann, E., Koons, P. O., Pavlis, T. L., Hallet, B., Barker, A., Elliott, J., et al. (2015). Cooperation among tectonic and surface processes in the St. Elias Range, Earth's highest coastal mountains. *Geophysical Research Letters*, *42*(14), 5838–5846. https://doi.org/10.1002/2015GL064727

Enkelmann, E., Zeitler, P. K., Pavlis, T. L., Garver, J. I., & Ridgway, K. D. (2009). Intense localized rock uplift and erosion in the St Elias orogen of Alaska. *Nature Geoscience*, *2*(5), 360–363. https://doi.org/10.1038/ngeo502

Falkowski, S., Ehlers, T., Madella, A., Glotzbach, C., Georgieva, V., & Strecker, M. (2021). *Detrital zircon (U-Th)/He thermochronometry data from the Leones Valley, Patagonian Andes*. GFZ Data Services. https://doi.org/10.5880/fidgeo.2021.027

Falkowski, S., & Enkelmann, E. (2016). Upper-crustal cooling of the Wrangellia composite terrane in the northern St. Elias Mountains, western Canada. *Lithosphere*, *8*(4), 359–378. https://doi.org/10.1130/L508.1

Farley, K. A., Wolf, R. A., & Silver, L. T. (1996). The effects of long alpha-stopping distances on (U-Th)/He ages. *Geochimica et Cosmochimica Acta*, *60*(21), 4223–4229. https://doi.org/10.1016/S0016-7037(96)00193-7

Fernandez, R. A., Anderson, J. B., Wellner, J. S., & Hallet, B. (2011). Timescale dependence of glacial erosion rates: A case study of Marinelli Glacier, Cordillera Darwin, southern Patagonia. *Journal of Geophysical Research*, *116*(F1), F01020. https://doi.org/10.1029/2010JF001685

Fosdick, J. C., Grove, M., Hourigan, J. K., & Calderón, M. (2013). Retroarc deformation and exhumation near the end of the Andes, southern Patagonia. *Earth and Planetary Science Letters*, *361*, 504–517. https://doi.org/10.1016/j.epsl.2012.12.007

Fox, M., Leith, K., Bodin, T., Balco, G., & Shuster, D. L. (2015). Rate of fluvial incision in the Central Alps constrained through joint inversion of detrital 10Be and thermochronometric data. *Earth and Planetary Science Letters*, *411*, 27–36. https://doi.org/10.1016/j.epsl.2014.11.038

Georgieva, V., Gallagher, K., Sobczyk, A., Sobel, E. R., Schildgen, T. F., Ehlers, T. A., & Strecker, M. R. (2019). Effects of slab-window, alkaline volcanism, and glaciation on thermochronometer cooling histories, Patagonian Andes. *Earth and Planetary Science Letters*, *511*, 164–176. https://doi.org/10.1016/j.epsl.2019.01.030

Georgieva, V., Melnick, D., Schildgen, T. F., Ehlers, T. A., Lagabrielle, Y., Enkelmann, E., & Strecker, M. R. (2016). Tectonic control on rock uplift, exhumation, and topography above an oceanic ridge collision: Southern Patagonian Andes (47°S), Chile. *Tectonics*, *35*(6), 1317–1341. https://doi.org/10.1002/2016TC004120

Glasser, N. F., Harrison, S., Schnabel, C., Fabel, D., & Jansson, K. N. (2012). Younger Dryas and early Holocene age glacier advances in Patagonia. *Quaternary Science Reviews*, *58*, 7–17. https://doi.org/10.1016/j.quascirev.2012.10.011

GLIMS Consortium. (2005). GLIMS Glacier Database, Version 1. Boulder, CO: NASA National Snow and Ice Data Center Distributed Active Archive Center. https://doi.org/10.7265/N5V98602

Glotzbach, C., Busschers, F. S., & Winsemann, J. (2018). Detrital thermochronology of Rhine, Elbe and Meuse river sediment (Central Europe): Implications for provenance, erosion and mineral fertility. *International Journal of Earth Sciences*, *107*(2), 459–479. https://doi.org/10.1007/s00531-017-1502-9

Glotzbach, C., Lang, K. A., Avdievitch, N. N., & Ehlers, T. A. (2019). Increasing the accuracy of (U-Th(-Sm))/He dating with 3D grain modelling. *Chemical Geology*, *506*, 113–125. https://doi.org/10.1016/j.chemgeo.2018.12.032

Glotzbach, C., van der Beek, P., Carcaillet, J., & Delunel, R. (2013). Deciphering the driving forces of erosion rates on millennial to million-year timescales in glacially impacted landscapes: An example from the Western Alps. *Journal of Geophysical Research: Earth Surface*, *118*(3), 1491–1515. https://doi.org/10.1002/jgrf.20107

Glotzbach, C., van der Beek, P. A., & Spiegel, C. (2011). Episodic exhumation and relief growth in the Mont Blanc massif, Western Alps from numerical modelling of thermochronology data. *Earth and Planetary Science Letters*, *304*(3–4), 417–430. https://doi.org/10.1016/j.epsl.2011.02.020

Grabowski, D. M., Enkelmann, E., & Ehlers, T. A. (2013). Spatial extent of rapid denudation in the glaciated St. Elias syntaxis region, SE Alaska. *Journal of Geophysical Research: Earth Surface*, *118*(3), 1921–1938. https://doi.org/10.1002/jgrf.20136

Guenthner, W. R., Reiners, P. W., Ketcham, R. A., Nasdala, L., & Giester, G. (2013). Helium diffusion in natural zircon: Radiation damage, anisotropy, and the interpretation of zircon (U-Th)/He thermochronology. *American Journal of Science*, *313*(3), 145–198. https://doi.org/10.2475/03.2013.01

Hallet, B. (1979). A theoretical model of glacial abrasion. *Journal of Glaciology*, *23*(89), 39–50. https://doi.org/10.3189/S0022143000029725

Hallet, B. (1996). Glacial quarrying: A simple theoretical model. *Annals of Glaciology*, *22*, 1–8. https://doi.org/10.3189/1996AoG22-1-1-8

Hallet, B., Hunter, L., & Bogen, J. (1996). Rates of erosion and sediment evacuation by glaciers: A review of field data and their implications. *Global and Planetary Change*, *12*(1–4), 213–235. https://doi.org/10.1016/0921-8181(95)00021-6

Haresign, E., & Warren, C. R. (2005). Melt rates at calving termini: A study at Glaciar León, Chilean Patagonia. *Geological Society, London, Special Publications*, *242*(1), 99–109. https://doi.org/10.1144/GSL.SP.2005.242.01.09

Harrison, S., Glasser, N., Winchester, V., Haresign, E., Warren, C., Duller, G. A. T., et al. (2008). Glaciar León, Chilean Patagonia: Late-Holocene chronology and geomorphology. *The Holocene*, *18*(4), 643–652. https://doi.org/10.1177/0959683607086771

Headley, R. M., & Ehlers, T. A. (2015). Ice flow models and glacial erosion over multiple glacial–interglacial cycles. *Earth Surface Dynamics*, *3*(1), 153–170. https://doi.org/10.5194/esurf-3-153-2015

Hein, A. S., Dunai, T. J., Hulton, N. R. J., & Xu, S. (2011). Exposure dating outwash gravels to determine the age of the greatest Patagonian glaciations. *Geology*, *39*(2), 103–106. https://doi.org/10.1130/G31215.1

Herman, F., Beaud, F., Champagnac, J.-D., Lemieux, J.-M., & Sternai, P. (2011). Glacial hydrology and erosion patterns: A mechanism for carving glacial valleys. *Earth and Planetary Science Letters*, *310*(3–4), 498–508. https://doi.org/10.1016/j.epsl.2011.08.022

Herman, F., Beyssac, O., Brughelli, M., Lane, S. N., Leprince, S., Adatte, T., et al. (2015). Erosion by an Alpine glacier. *Science*, *350*(6257), 193–195. https://doi.org/10.1126/science.aab2386

Herman, F., & Brandon, M. (2015). Mid-latitude glacial erosion hotspot related to equatorial shifts in southern Westerlies. *Geology*, *43*(11), 987–990. https://doi.org/10.1130/G37008.1

Herman, F., & Braun, J. (2008). Evolution of the glacial landscape of the Southern Alps of New Zealand: Insights from a glacial erosion model. *Journal of Geophysical Research*, *113*(F2), F02009. https://doi.org/10.1029/2007JF000807

Herman, F., & Champagnac, J.-D. (2016). Plio-Pleistocene increase of erosion rates in mountain belts in response to climate change. *Terra Nova*, *28*(1), 2–10. https://doi.org/10.1111/ter.12186

Hubbard, A., Hein, A. S., Kaplan, M. R., Hulton, N. R. J., & Glasser, N. (2005). A modelling reconstruction of the last glacial maximum ice sheet and its deglaciation in the vicinity of the Northern Patagonian Icefield, South America. *Geografiska Annaler: Series A, Physical Geography*, *87*(2), 375–391. https://doi.org/10.1111/j.0435-3676.2005.00264.x

Humphrey, N. F., & Raymond, C. F. (1994). Hydrology, erosion and sediment production in a surging glacier: Variegated Glacier, Alaska, 1982–83. *Journal of Glaciology*, *40*(136), 539–552. https://doi.org/10.3189/s0022143000012429

Jiao, R., Herman, F., Beyssac, O., Adatte, T., Cox, S. C., Nelson, F. E., & Neil, H. L. (2018). Erosion of the Southern Alps of New Zealand during the last deglaciation. *Geology*, *46*(11), 975–978. https://doi.org/10.1130/G45160.1

Koppes, M., Hallet, B., Rignot, E., Mouginot, J., Wellner, J. S., & Boldt, K. (2015). Observed latitudinal variations in erosion as a function of glacier dynamics. *Nature*, *526*(7571), 100–103. https://doi.org/10.1038/nature15385

Lang, K. A., Ehlers, T. A., Kamp, P. J. J., & Ring, U. (2018). Sediment storage in the Southern Alps of New Zealand: New observations from tracer thermochronology. *Earth and Planetary Science Letters*, *493*, 140–149. https://doi.org/10.1016/j.epsl.2018.04.016

Leutelt, R. (1932). Die Rolle der glazialen erosion im Formengebäude der Alpen. *Geologische Rundschau*, *23*, 31–38. https://doi.org/10.1007/BF01802498

Lukens, C. E., Riebe, C. S., Sklar, L. S., & Shuster, D. L. (2016). Grain size bias in cosmogenic nuclide studies of stream sediment in steep terrain. *Journal of Geophysical Research: Earth Surface*, *121*(5), 978–999. https://doi.org/10.1002/2016JF003859
Lukens, C. E., Riebe, C. S., Sklar, L. S., & Shuster, D. L. (2020). Sediment size and abrasion biases in detrital thermochronology. *Earth and Planetary Science Letters*, *531*, 115929. https://doi.org/10.1016/j.epsl.2019.115929
MacGregor, K. R., Anderson, R. S., & Waddington, E. D. (2009). Numerical modeling of glacial erosion and headwall processes in alpine valleys. *Geomorphology*, *103*(2), 189–204. https://doi.org/10.1016/j.geomorph.2008.04.022
Madella, A., Glotzbach, C., & Ehlers, T. A. (2021). How many grains are needed for quantifying catchment erosion from tracer thermochronology? *Geochronology Discussion* [preprint]. https://doi.org/10.5194/gchron-2021-6
Malusà, M. G., Resentini, A., & Garzanti, E. (2016). Hydraulic sorting and mineral fertility bias in detrital geochronology. *Gondwana Research*, *31*, 1–19. https://doi.org/10.1016/j.gr.2015.09.002
Massart, P. (1990). The tight constant in the Dvoretzky-Kiefer-Wolfowitz inequality. *Annals of Probability*, *18*(3), 1269–1283. https://doi.org/10.1214/aop/1176990746
McPhillips, D., & Brandon, M. T. (2010). Using tracer thermochronology to measure modern relief change in the Sierra Nevada, California. *Earth and Planetary Science Letters*, *296*(3–4), 373–383. https://doi.org/10.1016/j.epsl.2010.05.022
Melnick, D., & Echtler, H. P. (2006). Inversion of forearc basins in south-central Chile caused by rapid glacial age trench fill. *Geology*, *34*(9), 709–712. https://doi.org/10.1130/G22440.1
Mercer, J. H. (1976). Glacial history of southernmost South America. *Quaternary Research*, *6*, 125–166. https://doi.org/10.1016/0033-5894(76)90047-8
Preusser, F., Reitner, J. M., & Schlüchter, C. (2010). Distribution, geometry, age and origin of overdeepened valleys and basins in the Alps and their foreland. *Swiss Journal of Geosciences*, *103*(3), 407–426. https://doi.org/10.1007/s00015-010-0044-y
Raup, B., Racoviteanu, A., Khalsa, S. J. S., Helm, C., Armstrong, R., & Arnaud, Y. (2007). The GLIMS geospatial glacier database: A new tool for studying glacier change. *Global and Planetary Change*, *56*(1-2), 101–110. https://doi.org/10.1016/j.gloplacha.2006.07.018
Reiners, P. W. (2005). Zircon (U-Th)/He thermochronometry. *Reviews in Mineralogy and Geochemistry*, *58*(1), 151–179. https://doi.org/10.2138/rmg.2005.58.6
Reiners, P. W., Thomson, S. N., McPhillips, D., Donelick, R. A., & Roering, J. J. (2007). Wildfire thermochronology and the fate and transport of apatite in hillslope and fluvial environments. *Journal of Geophysical Research*, *112*(F4), F04001. https://doi.org/10.1029/2007JF000759
Riebe, C. S., Sklar, L. S., Lukens, C. E., & Shuster, D. L. (2015). Climate and topography control the size and flux of sediment produced on steep mountain slopes. *Proceedings of the National Academy of Sciences of the United States of America*, *112*, 15574–15579. https://doi.org/10.1073/pnas.1503567112
Riihimaki, C. A., MacGregor, K. R., Anderson, R. S., Anderson, S. P., & Loso, M. G. (2005). Sediment evacuation and glacial erosion rates at a small alpine glacier. *Journal of Geophysical Research*, *110*(F3), F03003. https://doi.org/10.1029/2004JF000189
Rivera, A., Benham, T., Casassa, G., Bamber, J., & Dowdeswell, J. A. (2007). Ice elevation and areal changes of glaciers from the Northern Patagonia Icefield, Chile. *Global and Planetary Change*, *59*(1–4), 126–137. https://doi.org/10.1016/j.gloplacha.2006.11.037
SERNAGEOMIN (2003). *Mapa Geológico de Chile: Versión digital* (Vol. 1, p. 1000000). Santiago, Chile: Servicio Nacional de Geología y Minería.
Shuster, D. L., Cuffey, K. M., Sanders, J. W., & Balco, G. (2011). Thermochronometry reveals headward propagation of erosion in an alpine landscape. *Science*, *332*(6025), 84–88. https://doi.org/10.1126/science.1198401
Shuster, D. L., Flowers, R. M., & Farley, K. A. (2006). The influence of natural radiation damage on helium diffusion kinetics in apatite. *Earth and Planetary Science Letters*, *249*(3–4), 148–161. https://doi.org/10.1016/j.epsl.2006.07.028
Singer, B. S., Ackert, R. P., & Guillou, H. (2004). 40Ar/39Ar and K-Ar chronology of Pleistocene glaciations in Patagonia. *Geological Society of America Bulletin*, *116*, 434–450. https://doi.org/10.1130/b25177.1
Starke, J., Ehlers, T. A., & Schaller, M. (2020). Latitudinal effect of vegetation on erosion rates identified along western South America. *Science*, *367*(6484), 1358–1361. https://doi.org/10.1126/science.aaz0840
Sternai, P., Herman, F., Valla, P. G., & Champagnac, J.-D. (2013). Spatial and temporal variations of glacial erosion in the Rhône valley (Swiss Alps): Insights from numerical modeling. *Earth and Planetary Science Letters*, *368*, 119–131. https://doi.org/10.1016/j.epsl.2013.02.039
Stock, G. M., Ehlers, T. A., & Farley, K. A. (2006). Where does sediment come from? Quantifying catchment erosion with detrital apatite (U-Th)/He thermochronometry. *Geology*, *34*(9), 725–728. https://doi.org/10.1130/g22592.1
Stübner, K., Drost, K., Schoenberg, R., Böhme, M., Starke, J., & Ehlers, T. A. (2016). Asynchronous timing of extension and basin formation in the South Rhodope core complex, SW Bulgaria, and northern Greece. *Tectonics*, *35*(1), 136–159. https://doi.org/10.1002/2015TC004044
Thomson, S. N., Brandon, M. T., Tomkin, J. H., Reiners, P. W., Vásquez, C., & Wilson, N. J. (2010). Glaciation as a destructive and constructive control on mountain building. *Nature*, *467*(7313), 313–317. https://doi.org/10.1038/nature09365
Tomkin, J. H., & Braun, J. (2002). The influence of alpine glaciation on the relief of tectonically active mountain belts. *American Journal of Science*, *302*(3), 169–190. https://doi.org/10.2475/ajs.302.3.169
Tranel, L. M., Spotila, J. A., Kowalewski, M. J., & Waller, C. M. (2011). Spatial variation of erosion in a small, glaciated basin in the Teton Range, Wyoming, based on detrital apatite (U-Th)/He thermochronology. *Basin Research*, *23*(5), 571–590. https://doi.org/10.1111/j.1365-2117.2011.00502.x
Tripathy-Lang, A., Hodges, K. V., Monteleone, B. D., & van Soest, M. C. (2013). Laser (U-Th)/He thermochronology of detrital zircons as a tool for studying surface processes in modern catchments. *Journal of Geophysical Research: Earth Surface*, *118*(3), 1333–1341. https://doi.org/10.1002/jgrf.20091
Ugelvig, S. V., & Egholm, D. L. (2018). The influence of basal-ice debris on patterns and rates of glacial erosion. *Earth and Planetary Science Letters*, *490*, 110–121. https://doi.org/10.1016/j.epsl.2018.03.022
Ugelvig, S. V., Egholm, D. L., & Iverson, N. R. (2016). Glacial landscape evolution by subglacial quarrying: A multiscale computational approach. *Journal of Geophysical Research: Earth Surface*, *121*(11), 2042–2068. https://doi.org/10.1002/2016JF003960
Valla, P. G., Shuster, D. L., & van der Beek, P. A. (2011). Significant increase in relief of the European Alps during mid-Pleistocene glaciations. *Nature Geoscience*, *4*(10), 688–692. https://doi.org/10.1038/ngeo1242
Vermeesch, P. (2007). Quantitative geomorphology of the White Mountains (California) using detrital apatite fission track thermochronology. *Journal of Geophysical Research*, *112*(F3), F03004. https://doi.org/10.1029/2006JF000671
Vermeesch, P. (2013). Multi-sample comparison of detrital age distributions. *Chemical Geology*, *341*, 140–146. https://doi.org/10.1016/j.chemgeo.2013.01.010
Wentworth, C. K. (1922). A scale of grade and class terms for clastic sediments. *The Journal of Geology*, *30*(5), 377–392. https://doi.org/10.1086/622910

Whipp, D. M., & Ehlers, T. A. (2019). Quantifying landslide frequency and sediment residence time in the Nepal Himalaya. *Science Advances*, *5*(4), eaav3482. https://doi.org/10.1126/sciadv.aav3482

Yanites, B. J., & Ehlers, T. A. (2012). Global climate and tectonic controls on the denudation of glaciated mountains. *Earth and Planetary Science Letters*, *325*(326), 63–75. https://doi.org/10.1016/j.epsl.2012.01.030

Yanites, B. J., & Ehlers, T. A. (2016). Intermittent glacial sliding velocities explain variations in long-timescale denudation. *Earth and Planetary Science Letters*, *450*, 52–61. https://doi.org/10.1016/j.epsl.2016.06.022